Norwegian University
of Life Sciences

Master's Thesis 2022 60 ECTS
Faculty of Environmental Sciences and Natural Resource Management

Determination of Elements in Snow and Water Samples on Jan Mayen

Thobias H. Østvedt
Master in Chemistry

Abstract

Iceland is considered one of the greatest dust emission sources in the Arctic. Once the dust is deposited, it significantly affects snow and ice albedo. This hastens the glacier melting and leads to new accessible dust sources priorly covered by snow and ice. To elucidate the effect of increased dust emission in high-latitude areas of the world, the HiLDA project was created. HiLDA aims to make a model for high-latitude dust emission and characterize the dust emission and transport processes using Iceland as a model source. During the summer of 2021, an expedition to Jan Mayen was conducted for sample collection, where among others, meltwater and snow samples were collected in a transect with a snow pit at 1300 m.a.s.l. These samples were analyzed for mercury- and multielement determination using Inductively Coupled Plasma - Mass Spectrometry (ICP-MS) and Inductively Coupled Plasma - Optical Emission Spectrometry (ICP-OES). A cold-vapor separation unit was used in tandem with ICP-MS during the mercury determination. Particles from one of the samples were examined with a Variable Pressure - Scanning Electron Microscope (VP-SEM). These analyses aimed to investigate the element concentrations in snow and meltwater on Jan Mayen, looking for trends in element concentrations in correlation with altitude and comparing the data with element concentrations found in data published in the literature.

The data showed that samples collected from altitudes above 1000 meters were less likely to be influenced by local dust and rather more likely by long-distance atmospheric dust. Elements commonly found in Icelandic basaltic dust, such as iron (Fe) and aluminum (Al), were negatively correlated with increasing altitude, with p-values below 10^{-05}. The back trajectories affecting Jan Mayen come from the north and southwest, which indicates that particles originating from Iceland can be a contributor to dust on Jan Mayen. Comparisons of aluminum and iron concentrations from the snow pit on Jan Mayen with data from the literature revealed approximately seven times higher concentrations in the ‘Jan Mayen samples’. The expected concentration range of mercury in Arctic snow was <10 ng/L, and 75% of the samples contained less than 10 ng/L. Single-particle characterization revealed fly ash in the sample, which suggests that computer-controlled electron microscopy can be used to estimate the anthropological contribution.

The elemental composition found in snow and water was unable to indicate dust sources due to Jan Mayen dust containing such large amounts of elements. Other sources had to be more predominant or contain elements not found in Jan Mayen dust to be determined as a source.

Sammendrag

Island er anerkjent som en av de største kildene i Arktis til atmosfærisk støv. Når støvet sedimenterer på snø og is påvirkes refleksjonsevnen til overflaten. Dette fører til raskere smelting av f.eks. isbreer, som leder til nedgang i refleksive overflater og øker tilgangen på tidligere tildekket støv. Prosjektet HiLDA ble opprettet for å forstå effekten av økt støvutslipp i nordlige breddegrader. HiLDA søker å lage en modell for støvutslipp og karakterisere transportprosessene atmosfærisk støv gjennomgår, med Island som modell. Det ble i 2021 holdt en ekspedisjon til Jan Mayen i regi av HiLDA for prøvetaking av blant annet snø-, smeltevann- og jordprøver. Prøvene ble samlet i en transekt fra toppen av Beerenberg, med en snøgrop på 1300 meter over havet. Prøvene ble analysert for kvikksølv- og flergrunnstoff-bestemmelse ved bruk av induktivt koblet plasma – massespektrometer (ICP-MS) og induktivt koblet plasma – optisk emisjonspektrometer (ICP-OES). Til kvikksølvbestemmelsen ble det brukt en kalddamp-separator for å skille prøven fra matriks. Partiklene fra en av prøvene ble observert med et varierende trykk–skanningelektronmikroskop (VP-SEM). Hensikten var å undersøke grunnstoffkonsentrasjonene funnet i snø- og smeltevannsprøver fra Jan Mayen, samt å teste for korrelasjon mellom konsentrasjoner og høyde. I tillegg var det et mål å sammenligne resultatene med data fra litteraturen.

Resultatene tydet på at prøver som var samlet fra over 1000 meters høyde var mindre sannsynlig å være påvirket av lokalt støv, men heller sannsynlig å være påvirket av langtransportert støv. Grunnstoff som finnes i islandsk basalt-støv, som jern (Fe) og aluminium (Al) var negativt korrelert med økende høyde, med p-verdier under 10^{-05}. Vindene som påvirker Jan Mayen blåser fra nord og sørvest, som indikerer at partikler fra Island kan være en bidragsyter til støv på Jan Mayen. Det ble funnet at jern- og aluminiumkonsentrasjonene var cirka 7 ganger høyere på Jan Mayen enn beskrevet i litteraturen. Den forventede kvikksølvkonsentrasjonen i arktisk snø var <10 ng/L, og 75% av 'kvikksølvprøvene' fra Jan Mayen inneholdt under 10 ng/L Hg. Karakterisering av enkeltpartikler med VP-SEM avdekket svevestøv i prøven, som antyder at data-kontrollert elektronmikroskopiering kan brukes til å estimere antropologisk bidrag av støv til Jan Mayen.

Grunnstoffsbestemmelsen i snø- og vannprøver kunne ikke brukes til å bestemme kilder til støv, da støvet på Jan Mayen viste seg å inneholde for mange grunnstoff til å kunne skilles fra andre kilder. For at andre kilder skulle oppdages måtte de inneholdt grunnstoff som ikke finnes i støvet på Jan Mayen.

Acknowledgments

This master thesis was completed as part of the Master's program in Chemistry at the Norwegian University of Life Sciences (NMBU). The study program is part of the Faculty of Chemistry, Biotechnology, and Food Science (KBM), but the work was conducted under the Faculty of Environmental Sciences and Natural Resource Manages (MINA).

First of I want to express my greatest gratitude to my two supervisors, Dr. Elin Lovise Folven Gjengedal from MINA at NMBU and Research Associate Professor Stine Eriksen Hammer from the National Institute of Occupational Health in Norway (STAMI). Thank you for the constant support and the reliability you both have provided during every step along the way. Thank you for your diligence, for your flexibility and for the great conversations we have had during this time. You are both great role models to me, and I am very lucky to have been getting your guidance.

I also want to thank the staff at NMBU-MINA who have directly helped me with the mercury- and multielement determination on the ICP-MS, especially Senior Engineer Karl Andreas Jensen, Senior Engineer Øyvind Enger, and Senior Engineer Solfrid Lohne. Your ability to think outside the box and your immense knowledge were of great value to this work. A great thank you to all the people in the lab that contributed to such a safe learning space and for making it a fantastic work environment. In addition, I also wish to express my gratitude to the people of HiLDA for letting me be part of this exciting study. I wish you nothing but success with the work that lies ahead.

Lastly, I wish to thank my family and my friends Espen Evju, Guro Ronglan Aarnes and Johan Tryti for being great, supportive friends during my five years at NMBU. Finally, a huge thank you to my partner Rebekka Moe. Thank you for being so supporting and encouraging during my time of writing.

Terms and abbreviations

Ag	Silver
Al	Aluminum
AMDE	Atmospheric Mercury Depletion Event
As	Arsenic
B	Boron
Ba	Barium
Be	Beryllium
Ca	Calcium
Cd	Cadmium
Ce	Cesium
Cl	Chlorine
Co	Cobalt
Cr	Chromium
Cs	Cesium
Cu	Copper
Dy	Dysprosium
EC/OC	Elemental Carbon/Organic Carbon
Er	Erbium
Eu	Europium
Fe	Iron
FIMS	Flow Injection Mercury System
Ga	Gallium
Gd	Gadolinium
Ge	Germanium
HCl	Hydrochloric Acid
HNO_3	Nitric Acid
Hf	Hafnium
Hg	Mercury
Hg^0	Elemental mercury
$Hg\text{-}CH_3$	Methylmercury

HiLDA	Iceland as a model for high-latitude dust sources – a combined experimental and modeling approach for characterization of dust emission and transport processes
Ho	Holmium
ICP-MS	Inductively Coupled Plasma – Mass Spectrometer
ICP-OES	Inductively Coupled Plasma – Optic Emission Spectrometer
K	Potassium
La	Lanthanum
Li	Lithium
LOD	Limit of Detection
LOQ	Limit of Quantification
Lu	Lutetium
m.a.s.l.	Meters above sea limit
Mg	Magnesium
Mn	Manganese
Mo	Molybdenum
Na	Sodium
$NaBH_4$	Sodium borohydride
Nb	Niobium
Nd	Neodymium
Ni	Nickel
NMBU	Norwegian University of Life Sciences
P	Phosphor
PAH	Polyaromatic hydrocarbons
Pb	Lead
PCA	Principal Component Analysis
PFAS	Per-and polyfluoroalkyl substances
Pr	Praseodymium
Rb	Rubidium
S	Sulphur
Sb	Antimony
Sc	Scandium
Se	Selenium

Si	Silicon
Sm	Samarium
Sn	Tin
$SnCl_2$	Stannous chloride
SO_4^{2-}	Sulfate
Sr	Strontium
Ta	Tantalum
Tb	Terbium
Te	Tellurium
Th	Thorium
Ti	Titanium
Tl	Thallium
Tm	Thulium
U	Uranium
V	Vanadium
VP-SEM	Variable-Pressure - Scanning Electron Microscope
W	Tungsten
Y	Yttrium
Yb	Ytterbium
Zn	Zinc
Zr	Zirconium

Table of Contents

1 Introduction

1.1 Background

Airborne dust particles from both anthropogenic and natural sources can travel great distances before depositing either as wet or dry deposition. Mineral dust is one of the major light-absorbing aerosols, and it will greatly affect snow and ice albedo when deposited, leading to acceleration of snow and glacier melting (Shi et al., 2021). This contributes to rising sea levels from melting glaciers and leads to less reflective areas, which in turn contributes to the increasing global temperature.

A greater prevalence of dust sources is expected in the future due to global warming (HiLDA, n.d.). Glaciers are retracting, and snow-covered areas are melting with the increasing temperature, which exposes more ground and increases the emissions of dust ultimately transported north in the Arctic. A model is necessary to estimate the effect of increased dust emission in high latitude areas, which led to the creation of the HiLDA project (Iceland as a model for high-latitude dust sources – a combined experimental and modeling approach for characterization of dust emission and transport processes). Iceland was selected as the model source as it is one of the greatest dust emission sources in the Arctic. The project is funded by the German Research Foundation DFG.

An expedition to Jan Mayen took place during the summer of 2021 to sample soil-, meltwater, and snow samples around the island. Samples were collected in a transect from the highest point of the island (2277 m.a.s.l.), as well as from a snow pit dug at 1300 m.a.s.l. Samples were also collected from random snow patches and meltwater around the island. The snow- and water samples are presented in this thesis, where the aim was to determine element concentrations using an Inductively Coupled Plasma – Mass Spectrometer (ICP-MS) and an Inductively Coupled Plasma – Optical Emission Spectrometer (ICP-OES). Snow and meltwater samples were also collected for mercury determination, to gain a better understanding of mercury deposition in the Arctic. In addition to the samples examined in this thesis, parallels were taken for determining the impact of anthropogenic activity, such as samples for determination of polyaromatic hydrocarbons, microplastic, and per- and polyfluoroalkyl substances. Polyaromatic hydrocarbons and per-and polyfluoroalkyl substances are known to be of anthropogenic origin.

Elements corresponding to Icelandic dust were of most significant interest, such as iron and aluminum. Elements giving information regarding pollution, such as mercury and lead, were also of interest. Trace elements were determined to provide fingerprints of elements in the dust, but also due to it being so little studied in snow.

1.2 Objectives for this thesis

The thesis includes one set of snow- and water samples for mercury determination and a parallel set of snow- and water samples for multielement analysis. Both sets of samples required an instrument that provided high accuracy and precision and that allowed for low detection limits. Available instruments such as the ICP-MS and ICP-OES fit perfectly for these analyses as they allow for low detection limits. The ICP-MS is preferred for samples with lower concentration ranges. In addition to these snow samples, particles from a third parallel set of samples were examined with a variable-pressure scanning electron microscope (VP-SEM).

The goal is to learn about the dust and particles found in snow and meltwater on Jan Mayen. This work aims to make a foundation of data regarding the element concentrations in snow and meltwater on Jan Mayen, as well as compare concentration levels with other snow samples described in the literature. Other than elements typically found in mineral dust, the sensitivity achieved by the ICP-MS allows for determination of rare earth elements in the snow and water samples, which there is currently little data of.

A major challenge with this task was recognizing what is dust from local sources, and what is potentially dust from external sources. Element determination may not be able to provide much more than indications of possible dust sources. However, combined with other analyses to be performed by other groups such as ion chromatography for anion determination (e.g., Cl^- and SO_4^{2-}) and gas chromatography coupled with mass spectrometry for polycyclic aromatic hydrocarbon determination, will provide a further understanding of the dust sources.

Hypotheses to be answered are:

- The mercury concentrations found in snow on Jan Mayen are in the range of <10 ng/L.
- Concentrations of elements associated with dust are negatively correlated to altitude.
- The elemental composition found in the snow and meltwater samples collected from different altitudes indicate the source as natural or anthropogenic; being local or long-range transport.

2 Theory

2.1 Jan Mayen

Jan Mayen is a volcanic island located 550 km northeast of Iceland, 500 km east of Greenland (71.08114°N, -8.1777°E). The island is part of Norway and has no permanent residents other than 14 members of the Norwegian military and four members of the Norwegian Meteorological Institute (Barr et al., 2021). The volcano Beerenberg reaches 2277 m.a.s.l. and is located on the northern side of the island. Glacial ice from the top of the volcano reaches down to sea level. The last great eruption on Jan Mayen was in 1970, although a minor eruption occurred in 1985 (Barr et al., 2021). The island is often divided into two parts: a southern- and a northern part. As the island is of volcanic origin, most of Jan Mayen is covered with volcanic sand and rocks at lower altitudes. Figure 2.1 presents two photos for reference, one taken from the southern part of Jan Mayen behind the research station (left) and one taken from the top of Nunataken, a bit more than halfway up Beerenberg (right).

Figure 2.1: *Left: Photo taken from the southern part of the island looking north with snow-covered Beerenberg in the background. Right: Photo taken from Nunataken (1550 m.a.s.l.) looking southwest. Photos by Stine E. Hammer (2021).*

Table 2.1 presents meteorological data from Jan Mayen summing up the weather of 2021.

***Table 2.1**: Information from the meteorological station at Jan Mayen from January to December 2021. The data is collected from the Norwegian Centre for Climate Services (Norwegian Centre for Climate Services, 2022a).*

	Temperature	**Precipitation**	**Mean wind speed**
Max/min values	13.8/-13.3 °C	106.6/4.5 mm	24.7/13.4 m/s
Month of max/min values	August/February	September/May	July/May
Mean	1.4 °C	51.2 mm	20.9 m/s

Data from the Norwegian Centre for Climate Services also shows that wind registered at Jan Mayen mainly comes from the north, north-northwest, and south-southwest (Norwegian Centre for Climate Services, 2022b). The strongest winds came from the north.

2.2 High latitude dust

2.2.1 Iceland as a dust source and environmental challenges

Iceland is one of the most significant sources of dust in the Arctic, having over 40,000 km^2 of desert areas (Dagsson Waldhauserova et al., 2017). It has been reported to have a dust suspension frequency of 135 dust days annually during the time period of 1942-2012 (Dagsson Waldhauserova et al., 2017). Not only is Iceland an island with volcanic activity, but in addition dust plumes influenced by high-intensity winds strongly contribute to dust emissions. The Icelandic dust is dark in color and consists primarily of volcanic glass rich in heavy metals such as iron and titanium (Dagsson Waldhauserova et al., 2017).

A great example of ash and dust emissions from volcanic activity in Iceland was in 2010 with the eruption of *Eyjafjallajökull*. This eruption famously led to great ash plumes canceling a lot of flights in Europe. The latest volcanic eruption in Iceland happened in March 2021 from the volcano *Fagradalsfjall* and lasted for six months. On average, there is an eruption every 3-5 years on Iceland (Arnalds et al., 2016).

The dust is transported by wind circulation in the atmosphere. The dust can be deposited either directly as dry deposition or act as ice nucleators leading to wet-deposition. The snow albedo

is impacted by impurities in snow due to dust deposition (Pey et al., 2020). The reduction in albedo leads to increased snow and ice melting in areas influenced by greater amounts of deposited dust. In addition to intensifying snow and glacier melting, atmospheric dust also influences atmospheric conditions that affect climate change, such as triggering cloud formation by acting as condensation nuclei, which makes it rain (Arnalds et al., 2016). The increased melting of glaciers will in time lead to retraction of the glaciers, revealing more dust sources. Another negative environmental impact of atmospheric dust is deposition of toxic elements with the dust.

2.2.2 Dust transport in the atmosphere

It has been observed that temperature inversions play a significant role in aerosol distribution (Thomas et al., 2019). Temperature inversions are characterized by reversal of the normal temperature behavior in the troposphere, where instead of temperature decreasing with altitude, it increases (Britannica, T., 2020). The inversion layer marks the point in altitude where the temperature starts decreasing with altitude again. This meteorological phenomenon usually happens during winter and is common in the Arctic, close to the sea (Thomas et al., 2019). As the inversion layers form in the troposphere, their altitude is dependent on the altitude of the tropopause, the atmospheric border between the troposphere and the stratosphere. The altitude of the tropopause decreases closer to the poles (Timmermans, 2022). It has been observed that during winter in the Arctic, more aerosols are trapped below inversion layers, indicating low-level transport of particles from lower latitudes in the Arctic (Thomas et al., 2019). In contrast, during springtime, accumulation of particles above the inversion layers has been detected, indicating long-range transport (Thomas et al., 2019).

2.3 Mercury in the Arctic – Sources, deposition, and environmental impact

Steffen et al. (2007) explain the behavior of mercury in the atmosphere. Mercury is known for its volatility and long-range atmospheric transport in the environment. Due to mercury evaporation being temperature-dependent, mercury tends to accumulate in colder regions where the evaporation rate is lower, and condensation from the atmosphere occurs more easily. Gaseous elemental mercury resides in the atmosphere, being transported by the global wind systems. In 1995 it was discovered a sudden drop in the gaseous elemental mercury concentrations during springtime in the Arctic. This phenomenon was determined to be an atmospheric mercury depletion event and happens through a series of photochemical initiated

reactions involving halogens in the atmosphere. Gaseous elemental mercury (Hg^0) is turned into a more reactive species that both associate with particles in the air and deposit with them or deposit directly to the polar environment. It has been presented by Steffen et al. (2007) that the mercury that deposits during atmospheric mercury depletion events occur at marine coasts.

According to Driscoll et al. (2013), the overall mercury emission to the atmosphere ranges from 6500 to 8200 ton per year, of which 4600 to 5300 ton per year are from natural processes and sources. These natural processes include emissions from volcanic activity and emissions from the ocean. The main anthropogenic source of mercury emissions is mercury-dependent artisanal and small-scale gold mining (Esdaile & Chalker, 2018). Other anthropogenic sources include combustion of bio- and fossil fuels such as coal. Inorganic mercury can be methylated to methylmercury ($Hg\text{-}CH_3$) by bacteria in the oceans, leading to increased levels of methylmercury in fish and aquatic animals (UN-Environment, 2019). The aquatic food chain leads to bioaccumulation and biomagnification of methylmercury in larger aquatic animals. The consumption of fish and marine animals is the primary source of exposure to methylated mercury to humans (UN-Environment, 2019).

2.4 Trace elements in Arctic snow - Natural and anthropogenic sources

Trace elements of non-local origin found in Arctic snow can be of anthropogenic and natural sources. The natural sources include dust storms, volcanic eruptions, rock weathering, and mineralization and are the major sources of trace elements (Siudek et al., 2015).

Anthropogenic sources of trace elements include industrial processes such as fossil (As, Cu, Co, Cr, V, Ni, Sb, Fe, Mn, Zn, Sn) and oil consumption (Mn, Pb, Fe, Ni), motor vehicle exhaust (Pb, Cu, Cr, Sn, Sb), smelting (Ni, Cu, As, Pb, Cd), iron/steel manufacturing (Cr, Mn, Ni, Co), and waste incineration (Pb, Zn) (Siudek et al., 2015). These sources are indicated by principal component analysis on the results of trace element quantification of snow samples from urban Polen by Siudek et al. (2015).

Sea spray contributes as a natural source of trace elements, especially to sites near the ocean. Spolaor et al. (2021) calculated the sea spray contribution of elements in snow collected from Hansbreen, Southwest Spitsbergen, Norway. Ions associated with sea spray were Ca, Sr, Mg, Na, K, Li, B, Rb, and U (Spolaor et al., 2021).

2.5 Instrumental theory of instruments used for element determination and single-particle characterization

2.5.1 Cold-vapor separation

Cold-vapor separation is a separation technique used for total mercury concentration determination, providing a complete separation from the sample matrix. The technique takes advantage of mercury's physical trait of being gaseous at room temperature in its elemental form, Hg^0, hence the name cold-vapor. Usually, the technique is coupled with atomic absorption spectrometry. However, in this thesis, it was coupled with an ICP-MS.

The sample is introduced to the separation system. At the same time, a reduction agent, usually $SnCl_2$ or $NaBH_4$, is applied to the system. The sample and the reductant are mixed in a mixing coil before entering a gas-liquid separation unit. The gas-liquid separator is constantly supplied an inert gas, e. g. argon, bringing the gaseous mercury further in the analysis, whereas the sample matrix goes to waste. Cold-vapor separation can yield great sensitivity, such as detection limits of a few parts per trillion using atomic absorption (Skoog et al., 2017).

2.5.2 Inductively Coupled Plasma – Mass Spectrometry (ICP-MS)

Inductively Coupled Plasma – Mass Spectrometry was first introduced in the 1980s and has since grown in popularity due to its ability to provide low detection limits for most elements, high sensitivity, and reasonably good accuracy and precision (Skoog et al., 2017).

For liquid samples, the sample is introduced to a nebulizer by e. g. flow injection, where the base principle is evaporation of the sample to a fine mist. There exist many different nebulizers, but the most used are concentric glass and cross-flow nebulizers (Gaines, 2019). Gaseous samples can be introduced to the ICP-MS by gas chromatography, supercritical fluid chromatography, and hydride generation (Skoog et al., 2017). Direct introduction of gaseous samples is also possible, e. g. direct coupling with a cold-vapor separation unit. Introduction of solid samples is made possible using techniques such as electrothermal vaporization, ablation using laser or electrical discharges, and slurry nebulization (Skoog et al., 2017).

The sample solution is nebulized into a fine aerosol mist and transferred into a spray chamber to prevent larger droplets (drop diameter >8 μm) enter the inductively coupled plasma (Gaines, 2019). The smallest droplets are carried by an inert gas, usually argon, to a plasma torch. The plasma is generated by a spark applied to the argon gas, ionizing some argon atoms and making Ar^+. A radio frequency generator provides oscillations of the argon ions and electrons, leading

to further ionization of argon, creating a plasma. The sample is in turn atomized and ionized in the plasma before being transferred further in the ICP-MS through the interface system.

The interface system consists of two cones: a sampling cone and a skimmer cone. Behind the sampling cone, the pressure is held at approximately one torr, in contrast to the atmospheric pressure on the side of the ICP-torch (Skoog et al., 2017). A pressure of less than 10^{-4} torr is required for the mass spectrometer (Skoog et al., 2017). The sampling cone is a water-cooled nickel cone with an orifice of <1.00 mm in its center. The plasma gas is transmitted through the orifice by the difference in pressure, where it is met by a skimmer cone. The pressure behind the skimmer cone is at the pressure of the mass spectrometer (10^{-4} torr). Further, the ions are separated from the argon carrier gas, photons, and molecules that may have entered the mass spectrometer by an ion lens system. These lenses accelerate and focus the positive ions via negative voltage, and the ions encounter a quadrupole mass analyzer (Skoog et al., 2017).

The quadrupole mass analyzer consists of four parallel rods serving of electrodes, two positive and two negatives. The electrodes are arranged such that the positive rods are in the same plane and the negative rods are in the same plane. Radio frequency and variable direct-current and voltages are applied to the electrodes. The alternating current pushes and pulls the positive ions, making them swerve through the rods in wave-like motions. The currents, both alternating and direct-current, are simultaneously increased, and it is by this increase of the currents that only ions of a particular mass to charge (m/z) ratio is allowed to pass through the rods without touching them and becoming neutral ions (Skoog et al., 2017).

Some ICP-MSs contain more than one quadrupole, with a collision cell between two quadrupoles. The collision cell allows for reaction and interaction with other gasses to remove or work around potential interferences. Different gas modes are used for different elements depending on potential interferences. For instance, in a triple quad ICP-MS, the reaction of an ion with an *n* m/z-ratio with oxygen in the collision cell can be isolated in the following quadrupole by only allowing ions with *n+16* m/z-ratios to reach the detector. Helium is used as collision gas to remove polyatomic interferences that have formed in the colder parts of the plasma. Ammonia can be used for charge transfer from interferences, creating NH_3^+ and removing the charge of the interferences with high ionization energy.

The most common detector used in routine experiments is the electron multiplier (Skoog et al., 2017). Positive ions from the mass selection system are drawn toward negatively charged dynodes, 'kicking' off electrons on impact. The electrons are then drawn towards the next

dynode, which is positively charged, and 'kicks' off additional electrons. This process repeats itself in a chain of up to 20 dynodes, amplifying the amounts of electrons at each dynode. The number of electrons is in the end read as an electrical signal. The ICP-MS used for multielement quantification in this thesis has a dual-stage discrete dynode detector. This kind of detector can read the signal both at the end of the chain and in the middle. With such a detector, one can measure samples of higher concentrations without overstimulating the detector in the end of the chain by using the first stage.

2.5.3 Inductively Coupled Plasma – Optical Emission Spectrometry, ICP-OES

Inductively coupled plasma – optical emission spectrometry uses the same system as the ICP-MS for liquid sample introduction to the plasma. In contrast to the ICP-MS, the ICP-OES operates with emission of photons from atoms and ions excited in the plasma. When the sample reaches the plasma, it is first desolvated, then atomized and ionized. Atoms and ions are both exited in the plasma, leading to the emission of characteristic wavelengths. These wavelengths make it possible to qualitatively determine elements and quantify based on their intensity.

The earliest ICP-OESs used *radial* or *side-on viewing* of the plasma for detection, but the more modern ICP-OESs give the possibility to use both radial and axial (*end-on viewing*) viewing (Boss & Fredeen, 1997). Axial viewing is advantageous when measuring lower concentrations, as it covers more of the plasma than radial viewing. In contrast, radial viewing is used when measuring samples with higher element concentrations. This is one of the ICP-OES's advantages over the ICP-MS, as only light interacts with the detectors of ICP-OESs. The ICP-MS offers lower detection limits but is more vulnerable to samples of high concentrations and must often have them diluted prior to analysis.

Atoms emit photons of wavelengths depending on the energy difference between the ground state of the exited electron and its exited state. Electrons of lower orbitals exited to the highest orbital of an atom will result in higher wavelengths than electrons exited to a lower orbital. This allows for selection of measured wavelengths based on the sample and possible interfering elements with overlapping wavelengths. To differentiate between the wavelengths of the emitted photons, a monochromator is installed between the plasma and the detector. A series of mirrors lead the photons to the monochromator from the plasma to the detector. When selecting emission lines (wavelengths), one should consider using the most sensitive emission line without possible optical interferences.

Detectors in modern ICP-OESs use solid-state transfer devices that us consists of pixels, creating charges of incoming photons that can be read by a computer. The two types of solid-state transfer devices used are Charge-Insertion Devices and Charge-Coupled Devices.

Spectral interferences involve overlap of wavelengths from the analyte and interfering elements. To avoid spectral interference, the best choice is usually to pick a different emission line for the analyte. Other methods include improving the resolution or by application of an interelement correction factor (Boss & Fredeen, 1997). Interelement correction is applied by measuring another emission line of the interfering element and applying a predetermined correction factor (Boss & Fredeen, 1997). Other interferences include ionization interferences, where the analyte is ionized in the plasma. This effect is most common in high concentrations of elements with low ionization energy. The high concentration of easily ionized analytes leads to more of the atoms being ionized (Rury, 2016). To counter this interference, the application of an ionization buffer, such as a high-concentration cesium solution, is advised. The high concentration of easily ionized cesium leads to a great increase in ions in the plasma, making fewer analyte atoms become ionized (Rury, 2016).

2.5.4 Variable Pressure – Scanning Electron Microscope, VP-SEM

Variable Pressure – Scanning Electron Microscopes consist of a high voltage power supply powering an electron gun often with a tungsten filament, releasing electrons accelerated towards the sample through a series of magnetic lenses under vacuum to an energy up to 30 keV (Skoog et al., 2017). A high vacuum ensures a free path for the electrons to the sample without collision with other molecules (Skoog et al., 2017). The size, shape, and position of the beam, called the primary electron beam, are adjusted by apertures, scan coils, and electromagnetic lenses. The interaction between the electron beam and the sample can provide information on topography, specimen composition, crystallography, electrical potential, and local magnetic fields (Goldstein et al., 1992).

The sample is placed in a sample chamber under vacuum. The easiest samples to study are samples that conduct electricity. A common practice for studying non-conducting samples is sputter-coating the samples with a metallic film, such as platinum (Skoog et al., 2017). Smaller particles do not require coating, but it is necessary for examination of larger particles.

Interaction between the primary electron beam with the sample results in e.g. backscatter electrons, secondary electrons, and X-rays (Skoog et al., 2017). Backscattered electrons are primary electrons that made it out of the sample surface after colliding with atoms, exiting with

almost the same energy as they originally had in the primary electron beam. This signal gives information about atom density, but little information about the topography, as backscatter electrons reach e. g. 1.5 μm into the sample if the beam energy is assumed to be 20 keV (Skoog et al., 2017). Secondary electrons are electrons dislodged by the primary electron beam and are produced from depths of 50 to 500 Å (Skoog et al., 2017). As such, secondary electrons give results regarding the topography of the sample.

X-ray photons are produced by both continuum X-ray production (*Bremsstrahlung*) and by dislodgement of electrons in the inner shells of sample atoms (Joubert, 2017). Bremsstrahlung arises when electrons from the primary beam are decelerated by the Coulombic field in sample atoms, leading to the emission of a photon with wavelength determined by the loss in electron energy (Joubert, 2017). Characteristic X-ray produced by dislodgment of inner shell electrons of sample atoms results in ions in an excited state. This leads to electrons of outer shells dropping to a lower shell to take the place of the missing electron (Joubert, 2017). The energy of the produced X-ray is equal to the energy difference between the two shells.

3 Materials and methods

3.1 Sampling

The snow samples were collected in a transect on the South-West side of Beerenberg (2277 m), with a snow pit at around 1300 meters above sea level. Additional snow and water samples were collected from snow patches, lakes and running water around the island. As of this, the samples from Jan Mayen are divided into “transect samples”, “snow pit samples” and “miscellaneous samples from around the island”. The sampling was done in a period of 18 days, with 12 days of active sampling.

To avoid contaminating the snow, all sampling was done in headwind. Transect and miscellaneous samples were collected wearing cotton suits. Snow pit samples were collected wearing particulate free suits and P2 masks. The reasoning behind the caution is that snow is very sensitive to trace levels of contamination due to its low impurity content (Avak et al., 2019). The metal-free sampling tubes (Labcon®) and the tubes used for ‘mercury samples’ (Sarstedt) were kept closed prior to sampling. The tools used for snow pit samplingwere cleaned using deionized water that was brought from the University Centre in Svalbard. A complete list of tools used can be found in table A1 in appendix A.

In total, 72 samples were collected for mercury determination, and 73 samples were collected for multielement determination. Among these were 14 field blanks, seven for both analyses. The field blanks were collected by opening and closing seven 5-mL Sarstedt tubes and seven 50-mL Labcon® tubes. Samples 36 and 51 of the ‘mercury samples’ went missing, and sample 18 of the ‘mercury samples’ was never collected. Sample 73 of the ‘mercury samples’ was not preserved by adding hydrochloric acid (HCl) and nitric acid (HNO_3) and was therefore considered unusable for mercury analysis. During analysis of the ‘mercury samples’, samples 43 and 61 were forgotten and never analyzed. Sample 45 of the multielement analysis samples was missing liquid content because of leakage, and only particles were left in the sample tube.

3.1.1 Transect sampling

Starting from the top of Beerenberg, going downwards heading south-west, different types of samples were collected. The first samples were collected at the top of the volcano at 2277 m.a.s.l. Figure 3.1 illustrates the transect route.

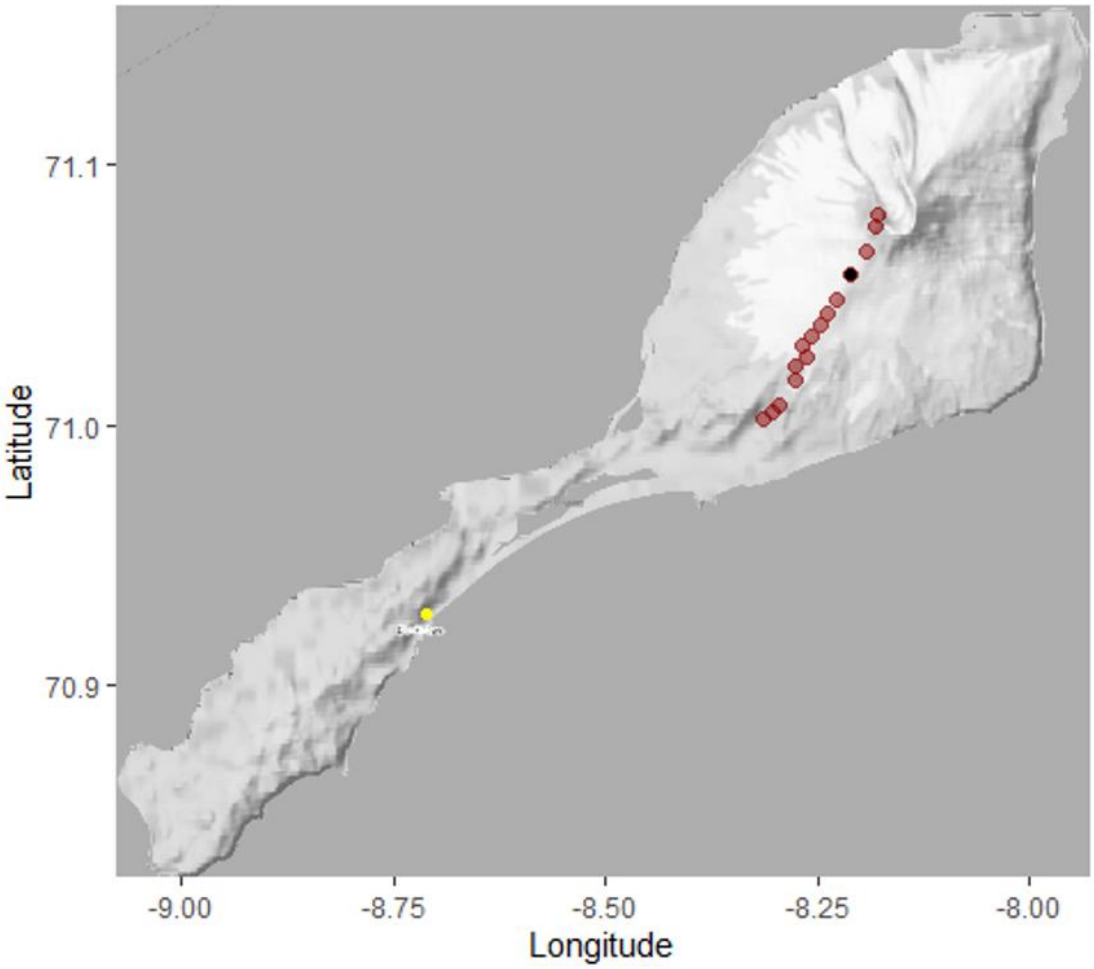

Figure 3.1 *Map of Jan Mayen with transect sample sites marked with red dots. The dark dot represents the location of the snow pit. In total, there were 15 sampling sites in the transect. Map constructed in R using ggmap (David Kahle and Hadley Wickham, 2013) and OpenStreetMap (OpenStreetMap contributors, 2017). The research station and base of operations is indicated by a yellow dot.*

Sampling was done by injecting sample tubes into the snow. For 'mercury samples', 5 mL Sarstedt tubes were used. Labcon® metal-free 50 mL tubes were used for the multielement analysis samples. A complete list of all samples collected and analyzed in this thesis can be found in table A2 in appendix A.

3.1.2 Snow pit sampling

The approach to digging the snow pit followed a protocol made by the Norwegian Polar Institute (Norwegian Polar Institute, 2018) and is summarized below.

Before sampling, snow density and temperature were measured, and melt layers were identified and measured. During sampling, particulate free suites, P2 masks, and sunglasses were worn,

as well as nitrile gloves (VWR). Before samples were taken, snow was first scraped off using a clean plastic crystal card. The depth was then measured, and the plastic tool was inserted horizontally. The sample tube was then inserted into the snow from above and pushed down until it hit the crystal card. This way, it was possible to determine the sampling depth. Samples were taken at 5 cm intervals to a depth of one meter. Unfortunately, the 'mercury sample' from the depth of 40-45 was missed. In total, 18 'mercury samples' and 19 'multielement samples' were collected, both sample series with additional seven blank samples.

3.2 Determination of total mercury in snow and water samples

The analysis was performed in September 2021 and was performed on two separate days. The 'miscellaneous samples' were analyzed on the first day, and the snow pit and transect samples were analyzed on the second day.

3.2.1 Visual observations and sample preparation

The 'mercury samples' were stored in a fridge at the research base during the sampling period. All 'mercury samples' had been added 69% HNO_3 (w/w) and 37% HCl (w/w) to concentrations of respectively 5 and 2 % (V/V) on Jan Mayen. Acid concentrations, sample tube information, and ICP-MS model information can be found in table A3 in appendix A. As the 'mercury samples' were already preserved with HCl, there was no need to store them in the freezer with the other snow samples. Adding HCl to the solution conserved the mercury in a chelating reaction, preventing any mercury from escaping. The sample volume varied between 2,4 to 5 mL. The amount of visible particles varied as well. Some samples were completely transparent with no visible particles, while others had a high content of sedimented particles at the bottom of the sample tube. The visible particles were not deemed part of the sample to be analyzed.

A red hue was observed on the snow surface in some places during sampling. This typical red color most likely came from red algae on the surface of snow.

3.2.2 Cold-vapor separation setup

It was expected that the mercury concentration would be less than 10 ng/L (Aspmo et al., 2006). To ensure high sensitivity, a setup consisting of a cold-vapor separation unit and an ICP-MS was used. The cold-vapor separation unit originated from a Perkin Elmer flow injection mercury system, FIMS 400. Figure 3.2.1 pictures the separation unit.

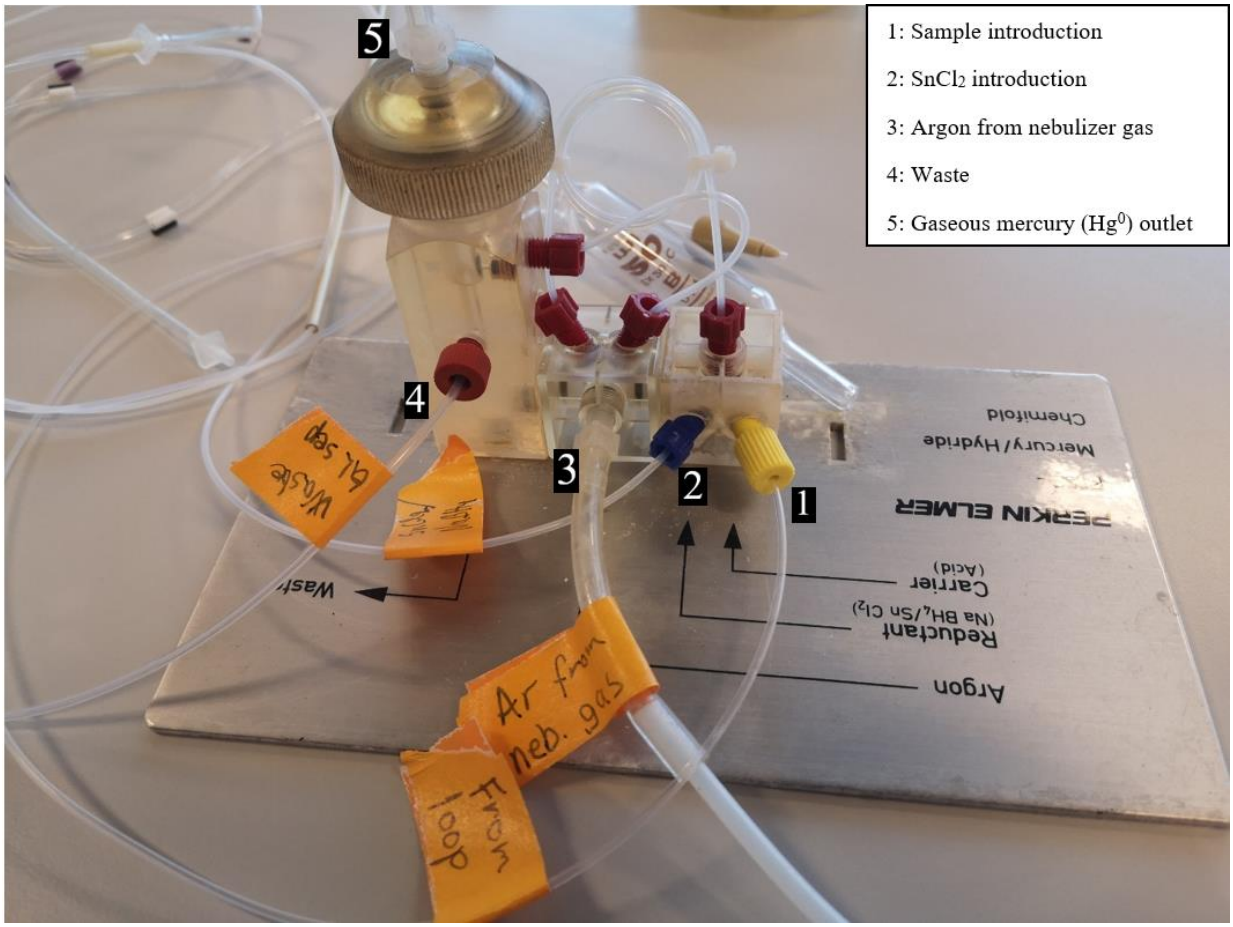

Figure 3.2.1: *Picture of the separation unit from a Perkin Elmer FIMS 400. The separation block is on the left. The numbers represent the different inlets and outlets of the separation system.*

Addition of 7% $SnCl_2$ (w/V) allowed for reduction of the Hg^{2+} to the gaseous form of mercury, Hg^0. The sample was mixed with the $SnCl_2$ in a loop from the mixing block first from the right in figure 3.2.1. The gaseous mercury would then be separated from the rest of the sample in the separation block. Argon gas blown through the separation block would bring the mercury to the ICP-MS. This could-vapor separation allowed for a complete separation of the analyte from the matrix in a closed system. A cut-off part of a 20 mL glass pipette was attached between the cold-vapor separation unit and the torch. This prohibited any droplets from the cold-vapor separation unit from entering the plasma and potentially extinguishing it. This part seemed useful, as some droplets were observed after some time. Figure 3.2.2 illustrates the connection to the ICP-MS.

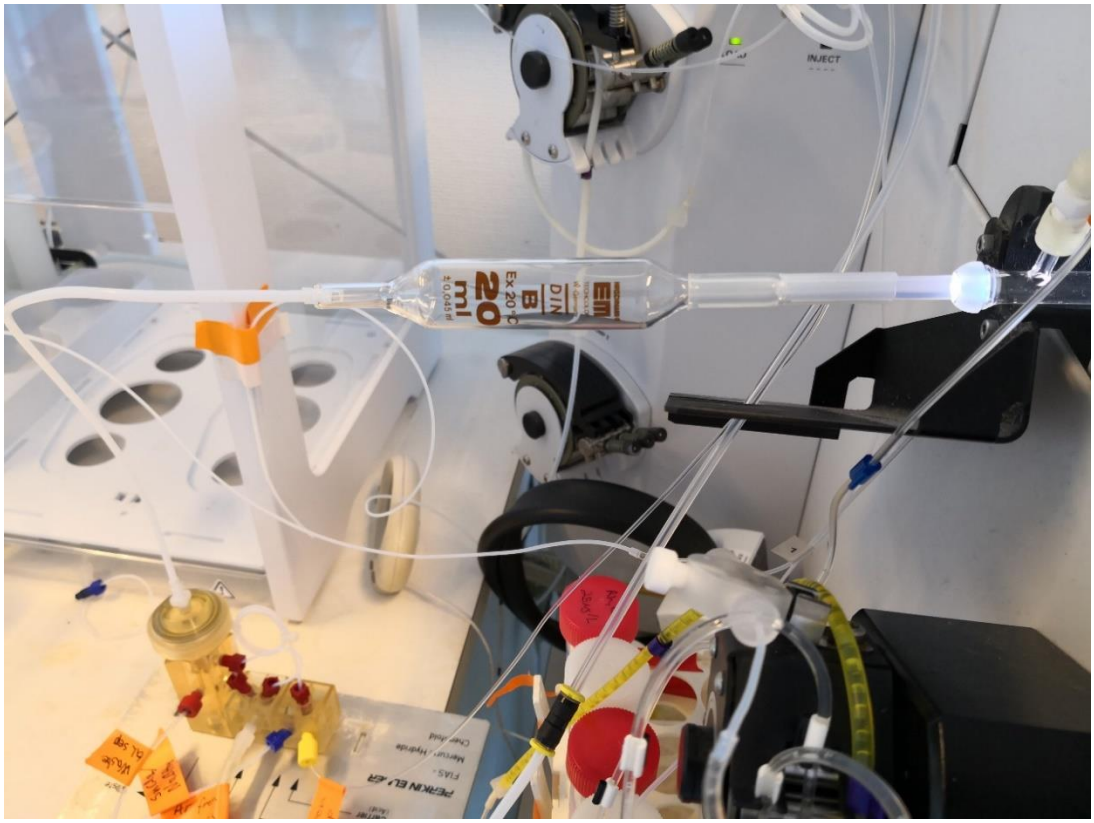

Figure 3.2.2: *The figure illustrates the connection of the separation unit to the ICP-MS using part of a 20 mL pipette as a drop collector to ensure a robust plasma. Foto by Karl Andreas Jensen.*

3.2.3 Standards, blanks, and reference materials

Given that the expected concentration levels were <10 ng/L, two Hg standards were prepared at 5 and 50 ng/L concentrations. The standards were acidified to the same concentrations as the samples diluted with deionized water. New standards were made on the second day of analyzing.

Field blanks collected on Jan Mayen were prepared at NMBU by acidifying to the same concentration as the samples. In contrast to the standards, the field blanks were prepared using the same acid as the 'mercury samples' brought back from Jan Mayen. The blanks were diluted to 5 mL using deionized water.

To control the method accuracy, three certified reference materials (CRM) were used. The three certified reference materials used were DORM-3, DOLT-5, and 1577c Bovine Liver. These reference materials were homogenized by decomposition in advance of the analyses. DORM-3 is fish protein with a mercury concentration of 0.382 ± 0.060 mg/kg (NRCC, 2008). DOLT-5 is made from dogfish liver, with a mercury concentration of 0.44 ± 0.18 mg/kg (NRCC,

2014). The 1577c bovine liver CRM contains 5.36 ± 0.17 µg/kg (NIST, 2016). DORM-3 and DOLT-5 were diluted 100 times. All CRMs were added HNO_3 and HCl to match the acid concentrations in the samples.

3.2.4 Mercury determination using ICP-MS

Table A4 in appendix A provides a complete overview of instrumental settings used during the analysis.

The samples were analyzed using an Agilent 8800 QQQ, with the cold-vapor separation unit attached between the autosampler and the torch on the ICP-MS.

Three masses were selected: ^{200}Hg, ^{201}Hg, and ^{202}Hg. Only no-gas mode was used, as there would only be Hg^0 that entered the ICP-MS from the sample. There was no need for any spray chamber or nebulizer in the sample introduction. The samples were analyzed using single quad mode.

Ten replicates per sample were analyzed with 50 sweeps/replicate. The probing dept of the autosampler was carefully adjusted to avoid solid particles being sucked up with the sample. Because of the small sample volumes, each sample could only be analyzed once. No methodical precision could be calculated. The only difference between the two analyses was a slight increase in load time, from 13 to 17 seconds, on day two of analyzing.

3.3 Multielement determination of snow and water samples

3.3.1 Visual observations and sample preparation

Multielement analysis samples were kept frozen (-16 °C) at Jan Mayen and was kept frozen (-20 °C) until sample preparation and analysis at NMBU. All samples from the expedition were packed together to keep them as cold as possible during transit from Jan Mayen.

The sample volume varied a lot, as well as the particle content. Sample 55 contained what looked to be part of some bryophyte.

The samples were thawed at room temperature and acidified according to Avak and co-authors (2019). This made ions attached to any surface, be it sample tube walls or particle surfaces, release and be accessible in the solution. Table A3 in appendix A provides an overview of acid concentrations as well as sample tubes used, tube volumes, and ICP-MS model information.

3.3.2 Initial concentration check

Before analyzing all the samples, five samples were picked out and analyzed to check the concentration levels. The samples include sample number 30, 36, 39, 47, and 61. They were transferred to 15 mL Sarstedt tubes and diluted 10 times to a total volume of 15 mL. After the initial concentration check, standards were prepared for the multielement determination.

3.3.3 Standards, blanks, and reference materials

The seven lab blanks were prepared using deionized water and acidified to the same concentration as the samples. The total volume in each blank sample was 50 mL.

Two certified reference materials and an in-house standard were used as accuracy measurements. The certified reference materials were 1640a (NIST, 2010) and 1643f (NIST, 2015). These are CRMs intended for analysis of trace elements in natural water. The in-house standard, 1643H, is a modified version of 1643e (NIST, 2004) with added concentrations of certain elements and was only used as a control for the standard curves. The reference materials were prepared in 50 mL polypropylene tubes and added HNO_3 to the same concentration as the samples. The reference materials were then diluted to 50 mL using deionized water. The CRMs 1640a and 1643f was diluted five times, and the house standard 1643H was diluted 10 times.

The CRMs did not contain the following elements: Sc, Ti, Ge, Y, Sn, Pr, Tb, Hf, Ta, and W. Thus, the accuracy of the determination of these elements is missing.

An internal standard was used during the analysis, consisting of 20 µg/L Rh, In, and Bi in 2 % HNO_3 (V/V) and 30 % ethanol (V/V). It was mixed "online" with the carrier in a 1+16 ratio.

Standards were prepared from a combination of multi-standards and single-element standards. A complete list of all standards used in this thesis can be found in table A5 in appendix A. Concentrations of the standards used in this analysis can be found in table A6 in appendix A. All standards were acidified to match the acid concentration of the samples and shaken vigorously. Two standards were used, as well as one calibration blank. The standards were prepared the day before the analysis.

3.3.4 Multielement analysis using Agilent 8900 ICP-MS

The complete list of elements and isotopes determined in the multielement analysis can be found in table A7 in appendix A along with the gas mode used for each isotope and isotopes in the internal standard. The analysis was performed on December 2nd, 2021. Prior to the analysis, sea water from Drøbak was run through the system to dirty the cones in the ICP-MS to increase

the sensitivity. In total, 66 samples, seven field blanks, two standards, and three reference materials were analyzed. The highest standard was used as a drift check and was analyzed after every 10 samples. The samples were analyzed using no-gas mode and with the reaction gases O_2, He, and NH_3. In total, 93 masses were analyzed. Six replicates per sample were analyzed with 10 sweeps per replicate. Table A8 in appendix A gives a complete overview of instrumental settings used during the analysis.

Several of the samples contained concentrations well above the concentration range of the standards. The samples used in the initial concentration check were all samples that contained little to no particles. Samples with concentrations above the highest standard were analyzed on an ICP-OES with new standards taking the high concentrations into account.

3.3.5 Multielement analysis using Agilent 5110 VDV ICP-OES

Instrumental settings used can be found in table A9 in appendix A.

Three multielement standards were prepared, with concentrations high enough to cover the concentration ranges acquired from the ICP-MS. The three standards had a 1:5:10 ratio and were acidified to 1% (V/V) HNO_3. A complete list of standards, concentrations, and wavelengths can be found in table A10 in appendix A. Three field blanks, CRM 1643F, and in-house standard 1643H are also included. The analysis took place on December 16th, 2021, and the standards were prepared the day before.

The samples were analyzed using an Agilent 5110 VDV ICP-OES. Samples 58, 59, 60, 68, and 69 were diluted 10 times by transferring 1,5 mL sample to 15 mL polypropylene tubes and diluting to 15 mL using deionized water and 69% HNO_3 (w/w) to a concentration of 1 % (V/V). Both the diluted and undiluted original samples were analyzed. The detector used in the ICP-OES described in this thesis was a Charge-Coupled Device. The detector used in the ICP-OES described in this thesis was a Charge-Coupled Device. Only radial detection was used, as lower concentrations were already determined on the ICP-MS.

3.4 Single-particle characterization using VP-SEM

Single-particle characterization of one of the samples was performed at STAMI – The National Institute of Occupational Health in Norway.

Two samples were selected for single-particle characterization using a Hitachi SU6600 Variable Pressure – Scanning Electron Microscope. About 2 mL sample was transferred using

3 mL disposable transfer pipettes from Sigma Aldrich to Merck polycarbonate Millipore 25 filters with pore size 0.8. The filters were in disposable funnel units from Eichrom Technologies (Lisle, USA) in a vacuum suction chamber for quick separation. While extracting the samples from the sample tubes, the pipettes were held slightly above the particles in the bottom of the tubes. This was done with caution to not collect too many particles. In total, four filters were prepared with different particle concentrations from the two samples. A vacuum pump was turned on for a few seconds, and the water was collected in sample tubes below the filters.

The filters were removed and placed in a heating chamber at 36 ˚C for about 2 hours. Only one of the filters was further prepared for examination using the VP-SEM. The sample was secured using carbon tape before being coated with platinum using a Cressington Sputter Coater. The sample was then inserted into the VP-SEM, and images were taken of the particles using secondary electron imaging. Working distance was set to 10.2 mm, and extra high tension voltage (15.0 kV) was turned on, allowing for SEI picturing and chemical structure determination using energy-dispersive X-ray (EDX). Some particles were analyzed using spot measurements, providing mass percentages in the selected areas. Four spots were measured on four different particles. Three detectors were utilized for secondary electrons, backscatter electrons, and EDX.

3.5 Statistical methods

The statistical methods used in this thesis were descriptive statistics and tests for correlation using Spearman's test. Only arithmetic means were used in descriptive statistics in this thesis. Tukey's test was also utilized for determining outliers for each element. As each sample represented a different spot on the island, no outliers were removed or treated like outliers. For the mercury determination, of the 60 samples, six samples were identified as outliers using Tukey's test, with an upper whisker determined to be 13 ng/L. This was performed using GraphPad Prism version. 9.2.0. (332). Spearman's correlation tests were performed using Excel. Spearman's test was utilized due to the lack of normal distribution in the data. The detection limits (LOD) and quantification limits (LOQ) were determined respectively as three and ten times the standard deviation of the blanks.

RStudio was used for creating maps of Jan Mayen and creating snow pit plots (RStudio Team, 2020), with the CRAN packages ggplot2 (Hadley Wickham, 2016) and ggmap (David Kahle

and Hadley Wickham, 2013). Map data is copyrighted by OpenStreetMap contributors and is available from http://www.openstreetmap.org.

4 Results

4.1 Quality of the analyses

4.1.1 Mercury determination

Considering mercury samples, the instrumental analysis resulted in values greater than the limit of detection for all the field blanks. There were no differences between the determined concentrations of the CRMs, and all were within the certified concentration ranges. A table presenting LOD and LOQ for every element is in appendix B (table B1). Out of all the mercury isotopes, ^{202}Hg was chosen as the representative isotope, as it had the lowest limits of detection and is the most abundant mercury isotope in nature. LOD and LOQ were determined to 0.27 ng/L and 0.90 ng/L (table B1, appendix B). The concentrations of the blanks ranged from 1.3 ng/L to 1.6 ng/L, with a median of 1.5 ng/L. All mercury samples contained mercury above the LOQ, and the content ranged from 1.5 ng/L to 72 ng/L, with a median of 3.5 ng/L.

4.1.2 Multielement determination

Multiple isotopes were measured in the multielement analysis using ICP-MS for some of the elements. When determining which isotope to present, factors such as LOD, LOQ, CRM results, and natural abundance were used.

When creating a dataset of the multielement determination results using ICP-MS and ICP-OES, the following flow chart was utilized to determine whether the ICP-MS- or ICP-OES-values should be used for each sample and element. The final dataset consisted of a combination of results from the ICP-MS analysis and the ICP-OES analysis.

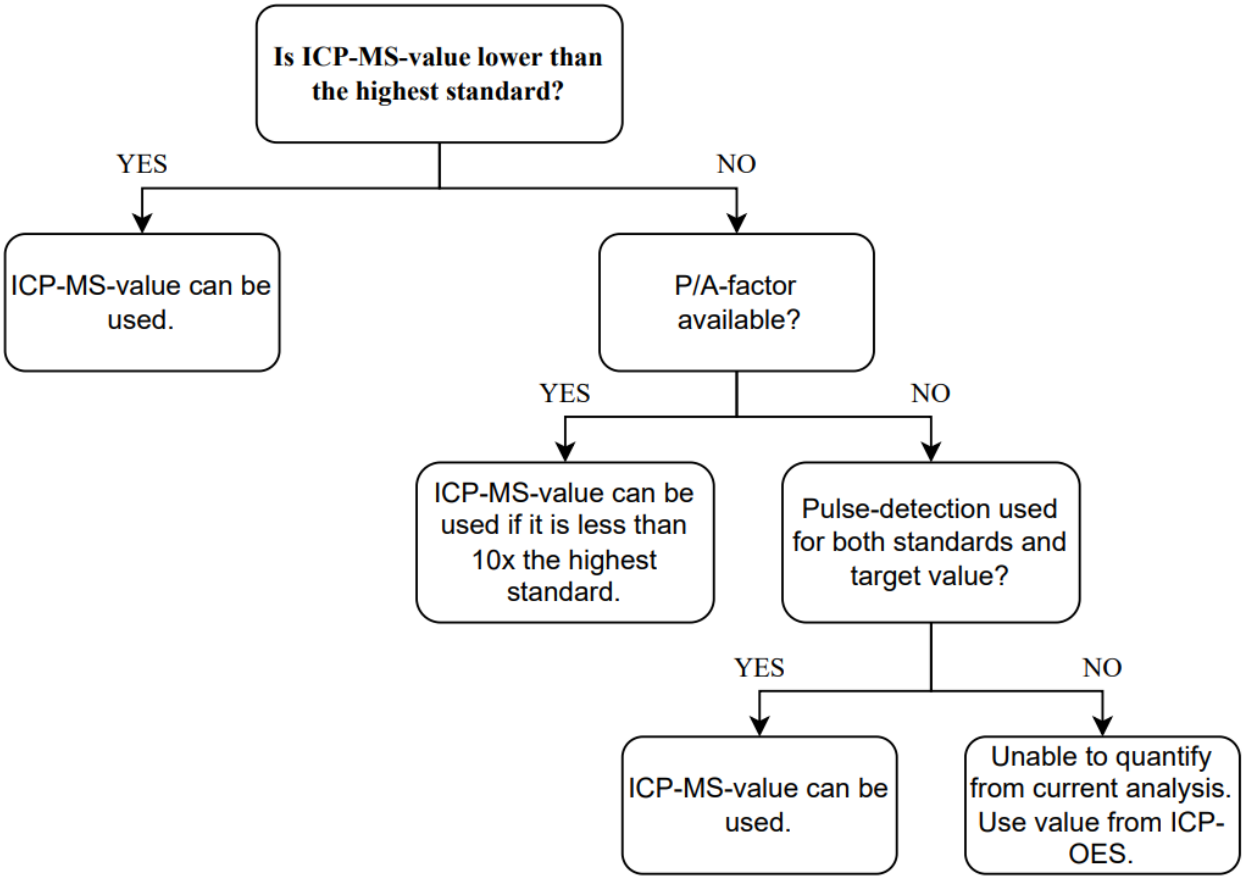

Figure 4.1: *Flowchart used for determination whether to use ICP-MS- or ICP-OES-value in the 'multielement results' dataset. The flowchart was used for each sample and each element.*

Trueness was regarded acceptable, as all elements but one with CRMs had at least one measured CRM value with bias of < 5%. This was not the case for niobium, with bias of 132 %. The CRMs did not contain the following elements: Sc, Ti, Ge, Y, Sn, Pr, Tb, Hf, Ta and W, and the accuracy of the determination of these elements was therefore unavailable.

Mostly all field blanks had values below LOD, and some elements had field blank concentration above LOD, but below LOQ. See table B1 in appendix B for all LOD and LOQ values. Field blank JM-034 was the only field blank to contain concentrations above LOQ. In total, 40 elements had field blank concentrations between LOD and LOQ, and six had field blank concentrations above LOQ.

4.2 Determination of total mercury in snow and water samples using ICP-MS and cold-vapor separation

Figure 4.2.1 provides an overview of the results from the mercury determination in the snow and water samples on Jan Mayen. A histogram of the mercury concentrations for each sample can be found in figure B1 in appendix B.

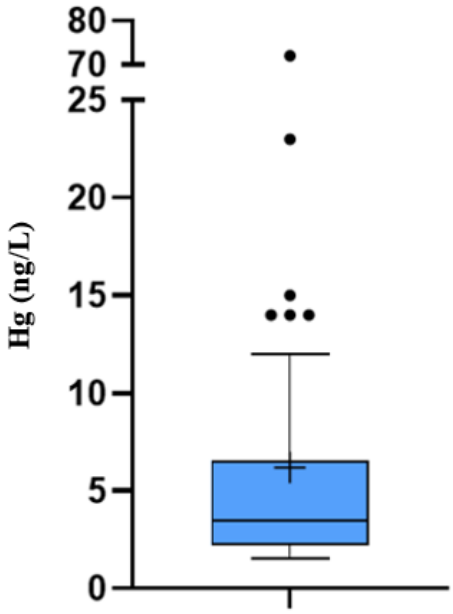

Figure 4.2.1: *The figure presents a boxplot of the results from the mercury determination in melted snow and water collected around the island. The median is at 3.5 ng/L mercury in melted snow amongst the 60 samples with an interquartile range (IQR) of 4.1 ng/L. The cross indicates the arithmetic mean.*

The boxplot presents the distribution of mercury concentrations, ranging from 1.5 ng/L to 72 ng/L. As the boxplot indicates, more than 75% of the samples contained mercury concentrations lower than 10 ng/L. The mean mercury concentration was 6.2 ng/L with a median of 3.5 ng/L.

To further comprehend the results, the samples are divided by sample type; “Transect samples”, “Snow pit samples”, and “Miscellaneous samples from around the island”, figure 4.2.2. ‘Transect samples’ were further divided into ‘Upper transect’ and ‘Lower transect’, where ‘upper transect’ samples originate from 1000 m.a.s.l. and above.

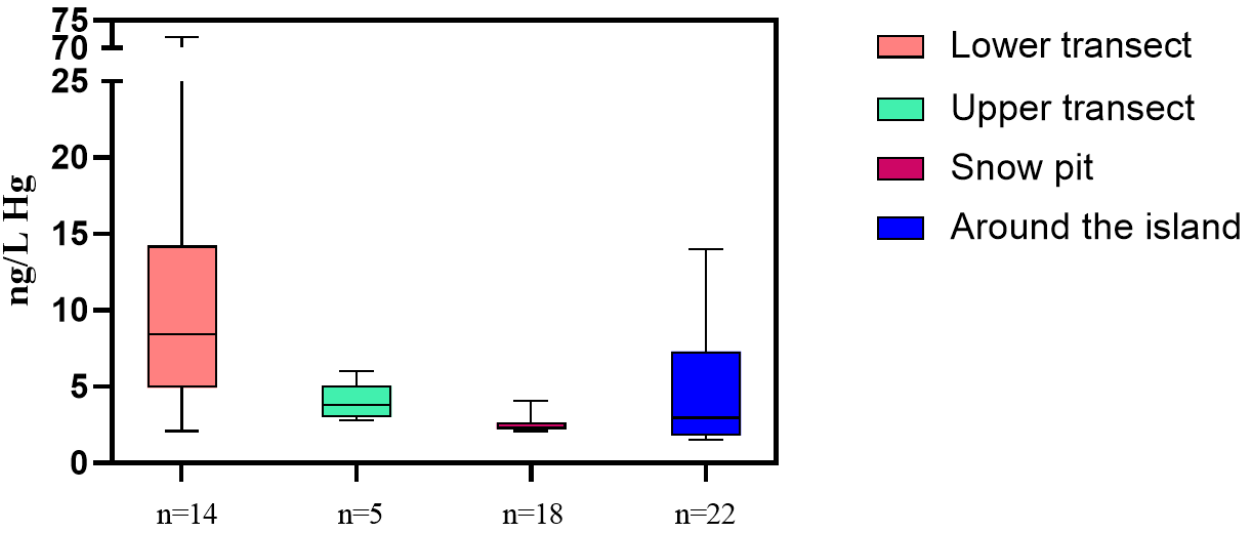

Figure 4.2.2: *Mercury concentrations from four different sampling areas: "Lower transect samples", "Upper transect samples", "Snow pit samples", and "Miscellaneous samples from around the island". The upper transect includes samples collected from 1000 m.a.s.l. and above. n annotates the number of samples for each sample type. The lines in the boxes represent the median value, and the whiskers indicate the minimum and maximum values.*

The least amount of variation between samples was found in the 'snow pit samples'. 'Lower transect samples' contained the most variation ranging from 2.1 ng/L to 72 ng/L. Compared to samples collected from the lower transect and random samples from around the island, 'snow pit samples' and 'upper transect samples' contained low amounts of variation. It should be noted that 'upper transect samples' only contained five observations. In addition, the 'lower transect samples' and the samples from around the island contained the highest mercury concentrations.

The mercury concentrations on Jan Mayen are also shown at the collected site in figure 4.2.3. The size of the circles corresponds to the mercury concentrations in ng/L.

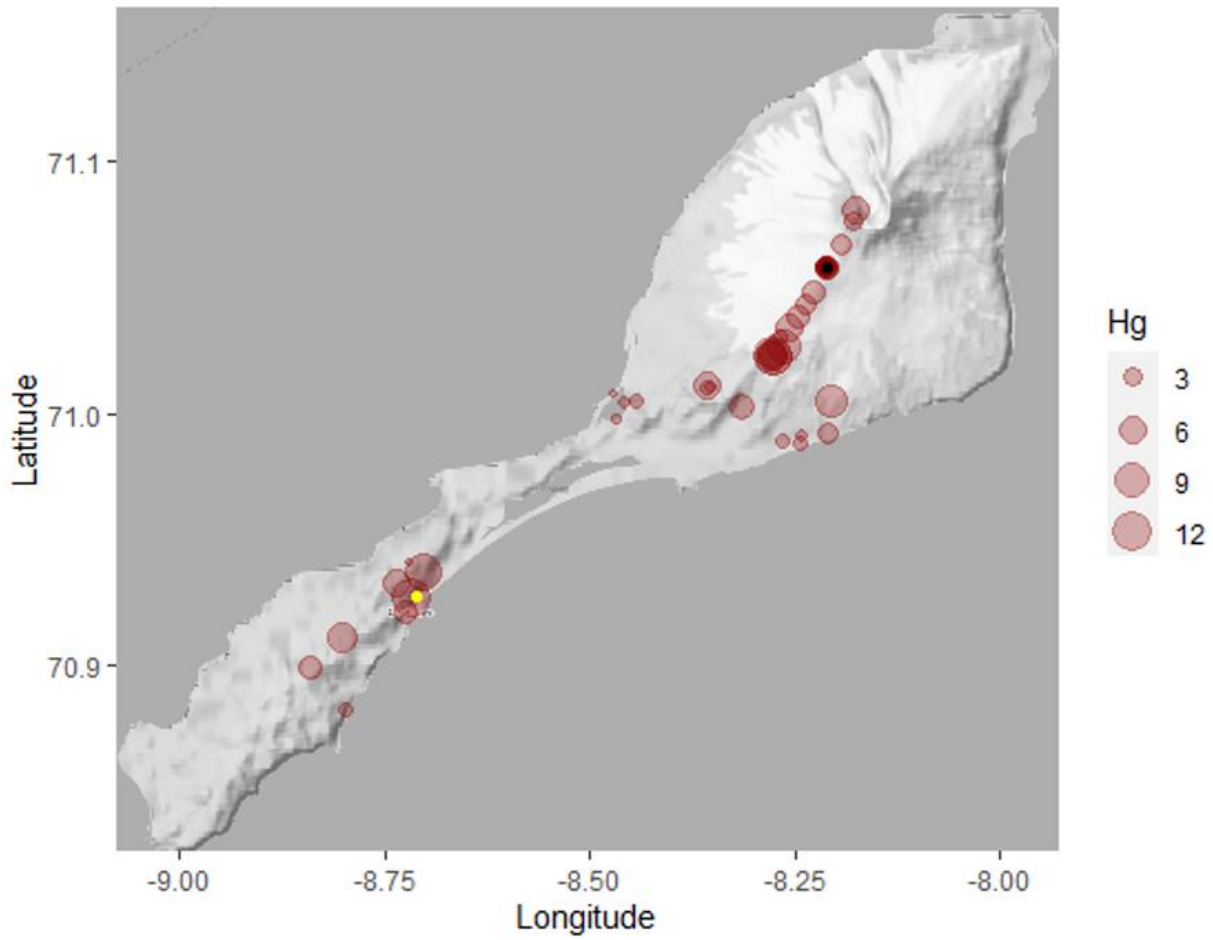

Figure 4.2.3: *Map of Jan Mayen with mercury concentrations plotted using sampling coordinates. The size of the dots represents the mercury concentrations in ng/L. The black dot indicates the site of the snow pit, and the yellow dot represents the research station. Map created in R using ggmap (David Kahle and Hadley Wickham, 2013) and OpenStreetMap (OpenStreetMap contributors, 2017).*

Spearman's correlation test resulted in a p-value of 0.985 when testing for correlation between mercury concentration in all samples and altitude. However, Spearman's correlation test resulted in a correlation between 'transect samples' and altitude, with a p-value of 0.00224. Comparing samples collected close to the research station with samples from further away, such as transect samples, can indicate whether human activity on Jan Mayen is a contributing factor. Considering the dots close to the research station are about the same size as the ones in the transect, great contribution from human activity on Jan Mayen is unlikely.

The mercury concentrations determined in the snow pit samples are visualized in figure 4.2.4. Melt layers were observed at depths of 7, 20, 33, and 52 cm, and ranged from 1 cm to 3 cm in thickness.

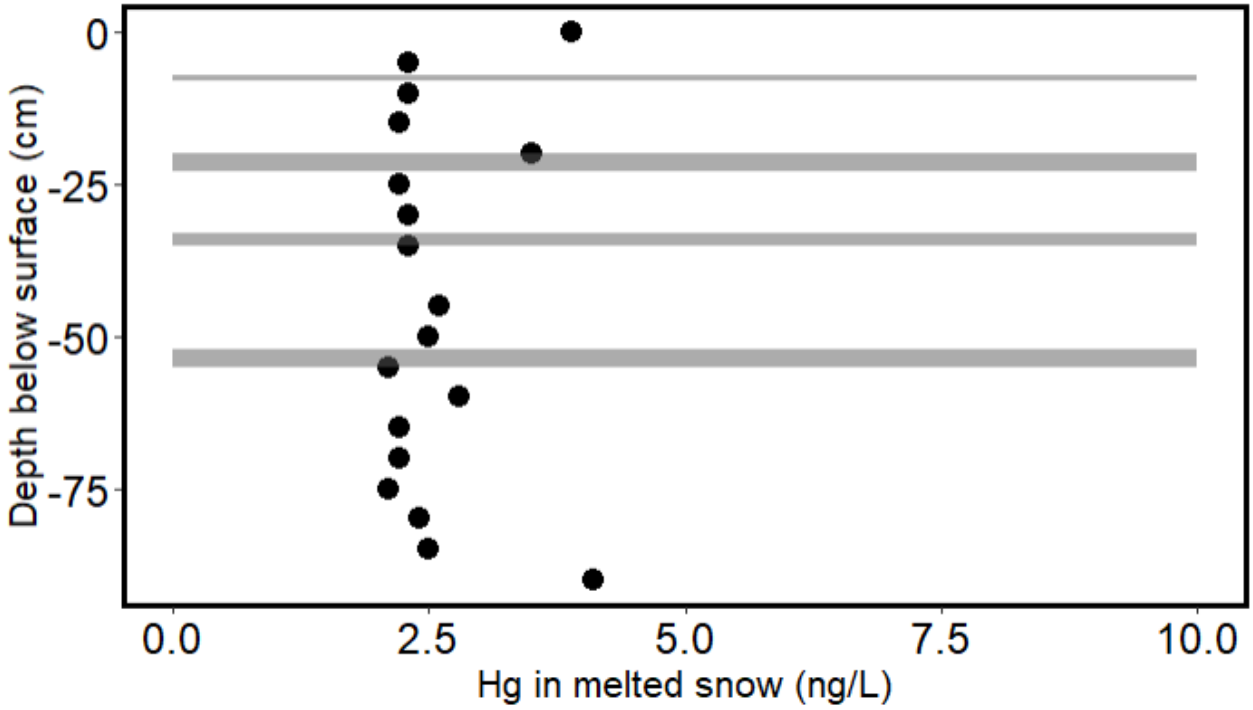

Figure 4.2.4: *Mercury concentrations in snow pit related to depth below surface. The shaded areas represent melt layers. Note that each dot represents five centimeter depth. The sample from the 40-45 cm depth is missing.*

Most samples contained approximately 2.5 ng/L mercury, whereas some samples close to the melt layers reached higher concentrations of 4 ng/L.

4.3 Multielement determination in snow and water samples using ICP-MS and ICP-OES

Table 4.3.1 includes percentages of samples with values below LOD and LOQ, as well as median and interquartile range (IQR).

Table 4.3.1: *Median, interquartile range (IQR), and percentages of values below the limit of detection (LOD) and limit of detection (LOQ)*[1].

Element	**Median** (µg/L)	**IQR** (µg/L)	**%<LOQ** (n=65)	**%<LOD** (n=65)	**Element**	**Median (µg/L)**	**IQR (µg/L)**	**%<LOQ** (n=65)	**%<LOD** (n=65)
Li	0.095	0.56	28	25	Mo	0.050	0.12	25	0
Be	0.013	0.081	29	25	Ag	<LOQ	---	77	51
B	<LOQ	---	91	82	Cd	0.0031	0.0088	31	25
Na	962	2032	0	0	Sn	0.026	0.042	32	11
Mg	539	2206	0	0	Sb	0.0065	0.0097	20	5
Al	692	5262	6	0	Te	0.00072	0.0017	43	26
Si	1597	5299	25	25	Cs	0.014	0.058	23	22
P	28	188	12	0	Ba	7.9	53	25	15
S	17	38	0	0	La	0.57	4.6	0	0
K	386	1535	25	15	Ce	1.1	7.9	18	18
Ca	610	3575	11	0	Pr	0.12	0.88	2	0
Sc	0.063	0.43	23	17	Nd	0.44	3.2	5	5
Ti	76	910	0	0	Sm	0.079	0.56	22	14
V	2.2	19	2	0	Eu	0.022	0.15	20	18
Cr	0.17	0.64	43	23	Gd	0.068	0.47	11	0
Mn	11	89	14	0	Tb	0.009	0.069	22	12
Fe	533	4899	6	0	Dy	0.050	0.34	17	0
Co	0.27	1.8	22	14	Ho	0.010	0.066	22	20
Ni	0.33	1.8	31	26	Er	0.026	0.17	22	18
Cu	1.0	3.9	28	20	Tm	0.003	0.022	29	28
Zn	0.79	4.8	32	12	Yb	0.021	0.14	22	12
Ga	0.14	0.88	22	20	Lu	0.0029	0.019	29	28
Ge	0.012	0.059	32	22	Hf	0.0029	0.013	29	26
As	0.035	0.12	17	2	Ta	0.0049	0.024	26	22
Se	<LOQ	---	57	38	W	0.013	0.027	23	17
Rb	0.90	4.5	20	20	Tl	0.0014	0.0070	38	28
Sr	7.0	47	0	0	Pb	0.17	1.4	35	28
Y	0.24	1.7	0	0	Th	0.031	0.11	22	14
Zr	0.16	0.71	5	0	U	0.031	0.14	22	22
Nb	0.073	0.17	22	15					

Of the 59 elements analyzed, 15 elements had 30% of the samples below LOQ. Three elements had over 50% below <LOQ, boron, selenium, and silver, respectively. As a result, their medians were <LOQ. Boron was the element with the highest number of values below LOQ, 91% <LOQ, respectively. Helsel (2012) recommends in the book *"Statistics for Censored Environmental Data Using Minitab and R"* reporting "the proportions of data below or above

[1] LOD and LOQ respectively calculated by 3 and 10 times the standard deviation of the blanks. IQR was determined by the difference between the upper quartile (3. Quartile) and the lower quartile (1. Quartile).

the maximum reporting limit, rather than estimating statistics that are unreliable" when over 80% of data is below the reporting limit (Helsel, 2012). These seven elements contained no censored data: Na, Mg, S, Ti, Sr, Y, and La.

Illustrations like figure 4.3.1 were created for each element. Values below LOD were substituted by 0.5x LOD, and values below LOQ were substituted by the value of LOQ.

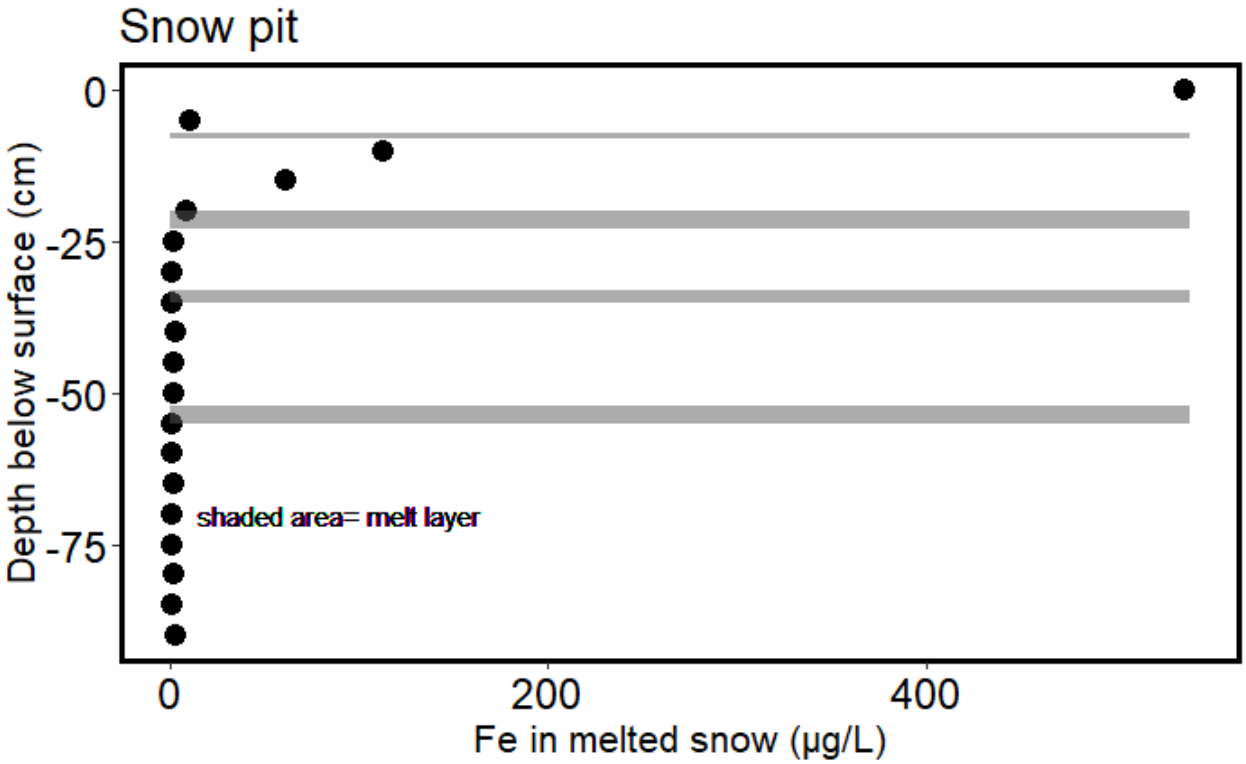

Figure 4.3.1: *Iron concentrations in snow pit as a function of depth. The shaded areas represent melt layers. Note that each dot represents a sample from five centimeter depth intervals, starting from 0 cm covering the 0-5 cm depth interval. This plot represents the typical concentration pattern for the elements determined in the snow pit samples.*

In general, snow pit concentration plots revealed highest concentrations above the 25 cm depth. This was however not the case for Na and S, which had highest concentrations around 50 cm depth. These two plots also contained a lot more variation than the other plots. The median value for Fe (presented in figure 4.3.1) was 533 µg/L, and the surface level sample in the snow pit was 537 µg/L. The concentration then drops to 10 µg/L right above the first melt layer. The following three samples contained descending Fe concentrations until the next melt layer. This trend was found to be for 46 of the 59 elements measured.

Among the samples collected above 1000 m.a.s.l., the mean Fe concentration was at 0.5 mg/L with a standard deviation of 0.51 mg/L, and similar for aluminum. In comparison, the Fe and Al concentrations from samples collected at 512 m.a.s.l. had respectively means and standard deviations of 8 ± 6.8 mg/L and 8 ± 7.7 mg/L. Correlation between Fe concentration in 'transect samples' and altitude was investigated using the Spearman's test ($\alpha = 0.05$), with a P-value of 1.324E-05. The same test was performed for aluminum, resulting in a correlation with a P-value of 4.956E-06.

4.4 Particle analysis results

Secondary electron imaging showed a multitude of different particles. Figure 4.4.1 displays some of these particles.

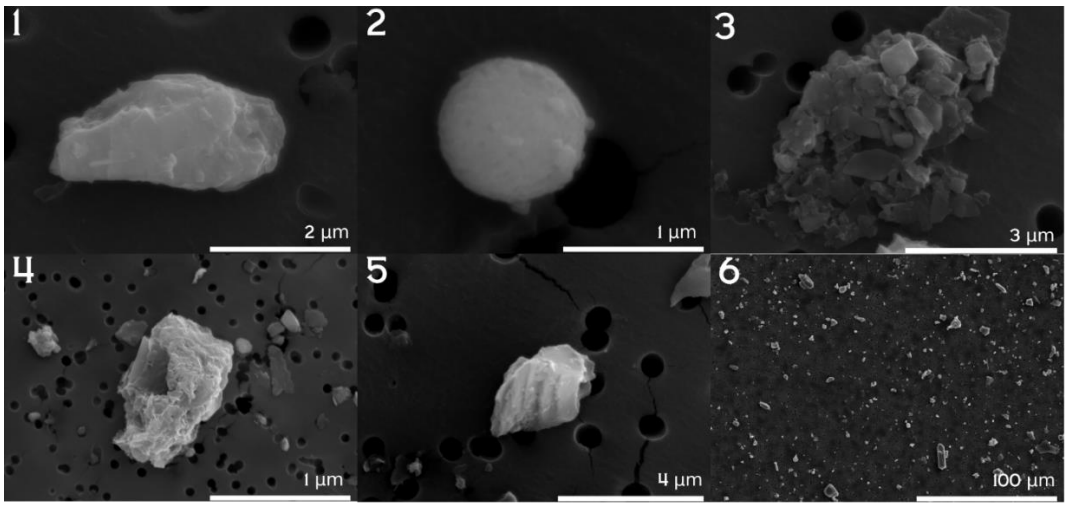

Figure 4.4.1: *Secondary electron images of different particles found in a sample collected at 512 m.a.s.l.*

Image six in figure 4.1.1 shows an overview of the particles found in the sample. The particle in image two shows a round particle with the characteristics of fly ash. In addition to the inorganic particles shown in image 1-5, some particles, most likely from biological material, was also observed.

In addition to imaging, spot measurements were taken using EDX. The results of the 12 spot measurements are provided in table 4.4.1. The spot measurements were not meant to be used to quantify the elements but rather as a qualitative analysis.

Table 4.4.1: *Normalized mass percentages for each of the 12 particles measured using spot measurements with energy-dispersive X-ray spectroscopy (EDX).*

Norm. mass percent (%)

Spectrum	C	O	Na	Mg	Al	Si	K	Ca	Ti	Fe	Cu	Zn	Pt
ROAF S04 36	33,08	40,27	4,00	-	3,93	10,18	-	-	-	0,51	-	-	8,03
JM 050 1	36,69	29,03	-	0,73	8,36	0,91	-	-	-	3,43	8,06	1,54	11,25
JM 050 2	36,22	28,22	-	0,75	9,22	0,95	-	-	-	3,70	9,43	2,09	9,41
JM 050 3	40,72	39,30	-	-	0,85	11,90	-	-	-	-	-	-	7,23
JM 050 4	24,53	41,34	2,82	0,58	5,86	15,27	3,18	-	-	-	-	-	6,41
JM 050 5	58,57	25,80	-	-	2,05	1,77	-	-	0,81	2,74	-	-	8,26
JM 050 6	34,13	36,77	1,14	1,20	2,89	6,90	0,62	1,67	0,89	3,12	-	-	10,67
JM 050 8	4,23	35,72	2,40	1,92	9,15	20,26	1,93	7,70	1,96	6,75	-	-	7,98
JM 050 9	40,96	36,63	1,73	0,53	2,76	7,80	-	-	-	0,71	-	-	8,89
JM 050 10	58,53	24,52	-	0,66	1,87	3,71	-	-	-	1,35	-	-	9,36
JM 050 11	44,33	33,02	0,65	0,74	2,67	6,22	-	-	-	2,26	-	-	10,10

Most if not all of the carbon mass originates from the carbon tape and the filter the particles were deposited on. Platinum originates from the platinum coating prior to the examination. Aluminum and silicium were detected in all the measured particles. Most of the particles contained iron and magnesium.

5 Discussion

5.1 Quality of the analyses

5.1.1 Quantification of total mercury in snow and water samples

The field blanks all contained levels of mercury above the detection limit (table B1, appendix B). Had the contamination been constant for all field blanks, subtraction from each sample would have been possible. It is unclear if this is the case because the field blanks were collected simultaneously. A possible explanation for the non-constant contamination could originate from the acidification during sampling. Frequent opening of the acid bottles in the field might have increasingly contaminated the acid, making the final samples the most contaminated. The field blanks were prepared last. A field blank from each day of conservation should have been made to avoid this, but this would have required bringing deionized water from the NMBU lab.

The accuracy of the analysis was deemed acceptable due to the CRMs being in range. None of the CRMs were snow reference materials, however, they were still used as indicators of the method's accuracy. This was decided as the CRMs were more complex solutions than melted snow and meltwater. If mercury could be determined accurately in the CRMs, the likelihood of accurate mercury determination in the samples would be very plausible. No method precision was achieved due to the low sample volumes available.

5.1.2 Multielement quantification in snow and water samples

The field blank JM-034 was consistently higher for all elements than the other field blanks. It is possible that the field blank might have been contaminated when it was prepared. Considering the acid and deionized water used was the same as for the other field blanks, the contamination must have come from elsewhere.

The use of ICP-OES was of great success for multielement determination in samples with high concentrations. Samples that were analyzed diluted and undiluted seemed to achieve nearly the same results.

Many of the samples contained visible particles sedimented in the bottom of the tubes. Prior to the analysis, it had to be decided whether these particles should be considered part of the sample or not. Due to the size of the particles, it was decided that the visible particles most likely originated from local sources on Jan Mayen. Due to their smaller size, the small long-distance transported dust particles would likely be available in the solution and not sedimented with the bigger presumably local source dust particles. Their small size would allow the small particles

to be nebulized and further decompose in the plasma. Filtering the samples was also considered but decided against due to possible loss of the smaller long-distance particles. Acid decomposition prior to filtering to dissolve all particles would add an extra step to the analysis, which potentially leads to contamination and loss of analyte. Acidification of the samples ensured that elements attached to the sample tube walls were accessible in the solution. A possible contribution to the element concentrations could have been the release of elements adsorbed to the sedimented particles in the bottom of the tubes. Some particles were presumably also solved during acidification. Samples containing great amounts of large particles also contained high element concentrations.

5.2 Mercury concentrations in snow and water samples

The expected mercury concentration was <10 ng/L, based on the measurements of snow and meltwater ponds on surface ice in the North Atlantic Ocean presented by Aspmo and co-authors (2006). More than 50% of the snow and water samples from Jan Mayen contained less than 10 ng/L. A corresponding mercury concentration range was found in snow on Svalbard by Bye T. (2019). In total, 85% of the samples contained mercury concentrations lower than 10 ng/L, but their samples all contained <10 ng/L. Most of the variation in our samples is found in the part of the lower transect and the samples from around the island. Figure 4.2.2 shows mercury concentrations of samples from the upper transect being generally lower than the samples from the lower transect. It is highly likely that mercury concentrations in the samples of lower altitudes are greater influenced by local dust due to the amount of volcanic sand observed on the lower altitude parts of the island. Figure C1 in appendix C presents a photo of Jan Mayen taken from the southern part of the island. Sand is seen blowing above the lower part of the transect towards Egg Island.

Spearman's correlation test of the mercury concentration in 'transect samples' indicates correlation with altitude, with a p-value of 0.00224. Further characterization of single particles will aid the understanding of the origin of the particles.

No contribution in mercury concentrations from human activity on Jan Mayen was detected. This conclusion derives from the mercury concentrations visualized by the circles around the research station in figure 4.2.3, being the same size as the circles at the bottom of the transect.

The mercury concentrations in the snow pit samples (figure 4.2.4) ranged from 2.1 to 4.1 ng/L. An observation to take note of is the increased concentrations found in samples close to the melt layers. Angor et al. (2016) present divalent mercury in snow in Dumont d'Urville, on the East Antarctic coast, being transported with snowmelt. A possibility may be that the mercury accumulates during melting, creating layers of higher mercury concentrations at depths of the melt layers. The sample from the deepest part of the snow pit contained the most mercury, with the surface sample containing almost the same amount. This sample was collected from the snow just above the glacial ice.

Further analysis of water isotopes in snow from the different depths of the snow pit will provide seasonal origin of the snow. These results are not available at the time of this thesis. Hopefully, these results reveal the seasonal time of the mercury deposition. Atmospheric mercury depletion events happen primarily in springtime (Steffen et al., 2007), and hopefully, these results reveal the seasonal time of mercury deposition.

5.3 Determined elements in snow and water samples

Most of the samples with values below the limits of detection or quantification were snow pit samples, especially from depths of 25 cm and below. This is shown in figure 4.3.1, presenting the distribution of Fe in the snow pit. The number of elements with samples reporting concentrations below LOQ or LOD (censored data) made statistical analyses challenging. Even descriptive statistics such as means and standard deviations were inaccessible for many elements without substituting the censored data. Helsel (2012) strongly recommends against substitution, with the lone exception being estimation of mean for data with one censoring limit. In this case, there are two censoring limits: LOD and LOQ.

Mean concentrations of the snow pit samples collected on Jan Mayen are compared with snow pit data collected by Avak et al. (2019) on *Weissfluhjoch*, Switzerland, in table 5.3.1. The values below the detection limit had been substituted with 0.5*LOD, which was the case for on average 10% of the measured values (Avak et al., 2019).

To be able to compare the results of the multielement quantification in the 'snow pit samples' from Jan Mayen with the results presented by Avak et al. (2019), the means were calculated with values below LOQ as if they were quantifiable. This was to match the protocol used by Avak et al. (2019) when calculating means and standard deviations for each element. Keeping

in mind that this includes high uncertainty for elements with high percentages of values below LOQ, such as Mn. None of the selected elements contained values below LOD from the 'Jan Mayen samples'.

Table 5.3.1: *Comparison of element concentrations in snow pit samples collected on Jan Mayen with snow pit samples from Weissfluhjoch analyzed and presented by Avak et al. (2019). n represents the sample size.*

Site		**Al (µg/L)**	**Ce (µg/L)**	**Fe (µg/L)**	**La (µg/L)**	**Mn (µg/L)**	**Nd (µg/L)**	**Pr (µg/L)**
Jan Mayen, Norway *(n=19)*	**Mean**	36	0.1	39	0.0	1	0.03	0.01
	Std. Dev	110	0.23	124	0.11	2.3	0.098	0.026
	%<LOQ	21	0	21	0	47	0	5
Weissfluhjoch, Switzerland ***(****n=324)*	**Mean**	4.870	0.014	5.990	0.0061	0.612	0.0077	0.0018
	Std. Dev	0.792	0.0029	1.180	0.0012	0.110	0.0017	0.00038

The elements provided in table 5.3.1 were selected based on a list of elements presented in Avak. et al. (2019), suggesting that at high alpine sites, these elements are mainly deposited with mineral dust (Avak et al., 2019; Gabrieli et al., 2011; Gabrielli et al., 2008). To correlate this with samples from the Arctic, the elements presented in table 5.3.1 are elements that have been found to have low sea spray contribution in the Arctic.

Spolaor et al. (2021) present results from a snow pit on Hansbreen (Southwest Spitsbergen), reporting sea-spray contribution percentages of a series of trace elements in the Arctic. The sea spray contribution for each element was calculated by using sodium as a reference element. These sea-spray contribution percentages were estimated for the following elements: K, Li, B, Rb, U, Ni, Co, As, Cs, Cd, Mo, Se, Se, Eu, Ba, V, Ga, Cr, P, Ti, Mn, Zr, Ce, Zn, Fe, Gd, Y, Pb, Bi, Yb, Al, Nb, Er, Nd, Dy, Sm, Ho, Th, La, Lu, Tm, Pr, Tb, In, Tl. Table 5.3.1 was created by presenting elements suggested to be mainly deposited with mineral dust, and that were estimated to have a low sea spray contribution (<1%).

Aluminum and iron concentrations were respectively 7.4 and 6.5 times higher in the snow pit on Jan Mayen compared with *Weissfluhjoch* (Switzerland), albeit with much larger variation. It is possible that part of the determined iron concentrations from the Jan Mayen snow pit

derives from Icelandic dust. The hypothesis is based on Icelandic dust primarily consisting of amorphous basaltic material with relative high Fe and Al content (Baldo et al., 2020). The snow pits on *Weissfluhjoch* were dug at greater altitudes than the snow pit on Jan Mayen (2536 m.a.s.l. vs. 1302 m.a.s.l.). Although considering the tropopause is lower closer to the poles, this should be negligable.

In 1997, Snyder-Conn et al. (1997) presented concentrations of soluble trace elements in Arctic Alaskan snow. Assuming that both the data presented by Snyder-Conn et al. (1997) and the data from the multielement determination presented in this thesis are log-normal distributed, one can derive that the median will be lower than the mean. By comparison of median values of trace elements determined from the snow and water samples on Jan Mayen, and the means presented by Snyder-Conn et al. (1997), it was found that the concentrations of aluminum, chromium, copper and iron were higher on Jan Mayen. This comparison depends on the assumption that both data sets are log-normal distributed. Otherwise, a comparison between medians and means would not be viable.

For a better understanding of the sources of the elements, analyses such as major ion determination using ion chromatography and determination of PAH and PFAS would likely be of benefit. These analyses are not performed at the time being but will be performed by other groups. Major ion determination may aid in estimating contribution from sea spray, and the presence of PAH and PFAS may indicate anthropogenic sources.

Based on the measurements reported by Hulth et al. (2010), an inversion layer over Jan Mayen was found at an altitude of about 1000 m.a.s.l. in 2008. Long-transportation of dust is mainly found at altitudes above the inversion layer (Thomas et al., 2019). Therefore, it is more likely to be more long-transported particles and organic matter in the samples collected at altitudes above 1000 m.a.s.l. However, this altitude may differ with the seasons. The snow pit was collected at ca. 1300 m.a.s.l., which is above this mark. Samples 1, 2, 3, 9, 36, and 37 were also collected above the suggested inversion layer.

In samples collected in the transect above the suggested inversion layer, iron and aluminium concentrations had average concentrations of 0.5 mg/L.

Samples from altitudes below 1000 m.a.s.l. had average iron and aluminum concentrations of respectively 7.4 mg/L and 8.1 mg/L. Correlation between both iron (P-value = 1.324E-05) and aluminum (P-value 4.956E-06) with altitude was found, where element concentrations decrease with altitude.

Characterization of the particle sources based on the elemental composition was not possible due to Jan Mayen dust containing such great amounts of elements. Other sources would not be noticeable unless they contained elements of high concentrations or elements not present in Jan Mayen dust. Determination of PAH, PFAS, and microplastic will hopefully work as fingerprints for anthropological sources. Ion chromatography can be used to determine levels of contribution from the ocean in the form of sea spray. These analyses are to be performed by other groups.

5.4 Single-particle characterization

The characterization of particles in one 'transect-sample' collected at 512 m.a.s.l. showed particles of different sizes and shapes (figure 4.4.1). Some of the particles were spherical with a diameter of about 1 μm, which is characteristic of fly ash. These are particles with anthropogenic origin produced from e.g. coal combustion in thermal power plants (Soni et al., 2020). Computer-controlled electron microscopy can be used to characterize a high number of particles determining e.g. the amount of fly ash in each sample (Eriksen Hammer et al., 2019). It would also yield the possibility to classify dust particles, but some particle types like soot would only be classified by operator-controlled SEM. Another possibility is to determine elemental carbon and organic carbon, as different Elemental Carbon/Organic Carbon (EC/OC) ratios can be used to predict sources of pollution (Qi et al., 2018). Studies by Chen et al. (2006) suggest that an EC/OC ratio of 2.5-10.5 indicates coal combustion (Chen et al., 2006). The downside with EC/OC analysis compared to single-particle SEM analyses is that it requires a much greater sample volume (5 L), and samples of such quantities were not collected. This would be a suggestion for further work.

6 Conclusion

The presented work covers the element determination of snow- and water samples collected on Jan Mayen. The cold-vapor separation technique in tandem with ICP-MS led to low detection limits with little to no interference from the matrix. Due to possible contamination of the acid used in 'mercury sample' preparation, the field blanks reported values above LOD and LOQ. However, the mercury concentrations in the samples matched the concentration range of <10 ng/L that was expected of snow samples in the Arctic, based on the findings of Aspmo et al. (2006). There was most variation between the samples at the lower parts of the transect and amongst the samples collected from random sampling sites around the island. The snow pit measurements showed mercury concentration accumulated around the melt layers. Due to a missing sample, no further conclusions could be drawn.

The high amount of censored data limited much statistical analyses of the determined element concentrations. This was expected due to snow's low impurity content (Avak et al., 2019). Only seven elements contained no censored data. Most of the censored data was due to low concentration levels in samples from the snow pit. For most elements, snow at depths below 25 cm contained concentrations below LOD or LOQ.

It was also found that concentrations were negatively correlated to increasing sampling altitude for elements such as Fe and Al. This was expected, as less local dust will reach higher altitudes by local winds due to a registered inversion layer at ca. 1000 m.a.s.l (Hulth et al., 2010). The samples from the snow pit had higher iron and aluminum concentrations on Jan Mayen than on *Weissfluhjoch* in Switzerland.

Due to dust on Jan Mayen containing such large amounts of different elements, source determination based on elemental composition was difficult. Local dust is likely a much more significant contributor to the concentrations found in the samples, more so than other natural and anthropogenic sources. Hopefully, other analyses to be performed by other groups such as PAH-, PFAS-, microplastic-, and major ion determination will be better indicators of anthropogenic sources.

Multiple particles of fly ash were detected during single-particle characterization using VP-SEM. A suggestion for further studies is computer-controlled electron microscopy to determine the amount of fly ash in each sample, which can be used to estimate anthropogenic contribution of deposited dust. Determination of EC/OC-ratios in snow samples could help further

understand the origin of the deposited dust, however, this would require a much higher sampling volume.

7 References

Arnalds, O., Dagsson-Waldhauserova, P., & Olafsson, H. (2016). The Icelandic volcanic aeolian environment: Processes and impacts—A review. *Aeolian Research*, *20*, 176–195. https://doi.org/10.1016/j.aeolia.2016.01.004

Aspmo, K., Temme, C., Berg, T., Ferrari, C., Gauchard, P.-A., Fain, X., & Wibetoe, G. (2006). Mercury in the Atmosphere, Snow and Melt Water Ponds in the North Atlantic Ocean during Arctic Summer. *Environmental Science & Technology*, *40*(13), 4083–4089. https://doi.org/10.1021/es052117z

Avak, S. E., Trachsel, J. C., Edebeli, J., Brütsch, S., Bartels-Rausch, T., Schneebeli, M., Schwikowski, M., & Eichler, A. (2019). Melt-Induced Fractionation of Major Ions and Trace Elements in an Alpine Snowpack. *Journal of Geophysical Research: Earth Surface*, *124*(7), 1647–1657. https://doi.org/10.1029/2019JF005026

Baldo, C., Formenti, P., Nowak, S., Chevaillier, S., Cazaunau, M., Pangui, E., Di Biagio, C., Doussin, J.-F., Ignatyev, K., Waldhauserova, P., Arnalds, O., Mackenzie, A., & Shi, Z. (2020). Distinct chemical and mineralogical composition of Icelandic dust compared to northern African and Asian dust. *Atmospheric Chemistry and Physics*, *20*, 13521–13539. https://doi.org/10.5194/acp-20-13521-2020

Barr, S., Thuesen, N. P., & Bangjord, G. (2021). *Jan Mayen*. Store Norske Leksikon. https://snl.no/Jan_Mayen

Boss, C. B., & Fredeen, K. J. (1997). *Concepts, Instrumentation, and Techniques in Inductively Coupled Plasma Optical Emission Spectrometry* (Second). Perkin Elmer.

Britannica, T. (2020). Temperature inversion. In *Encyclopedia Britannica* (Editors of Encyclopaedia). https://www.britannica.com/science/temperature-inversion

Bye, T. (2019). Capture Mechanisms of Mercury in Arctic Snow. *Master Thesis, NTNU*. http://hdl.handle.net/11250/2624232

Chen, Y., Zhi, G., Feng, Y., Fu, J., Feng, J., Sheng, G., & Simoneit, B. R. T. (2006). Measurements of emission factors for primary carbonaceous particles from residential raw-coal combustion in China. *Geophysical Research Letters*, *33*(20). https://doi.org/10.1029/2006GL026966

Dagsson Waldhauserova, P., Meinander, O., Olafsson, H., & Arnalds, O. (2017). Iceland as the largest source of natural air pollution in the Arctic. *EGU General Assembly Conference Abstracts*, 8508.

David Kahle and Hadley Wickham. (2013). ggmap: Spatial Visualization with ggplot2. *The R Journal*, *5(1)*, 144–161.

Driscoll, C. T., Mason, R. P., Chan, H. M., Jacob, D. J., & Pirrone, N. (2013). Mercury as a Global Pollutant: Sources, Pathways, and Effects. *Environmental Science & Technology*, *47*(10), 4967–4983. https://doi.org/10.1021/es305071v

Eriksen Hammer, S., Ebert, M., & Weinbruch, S. (2019). Comparison of operator- and computer-controlled scanning electron microscopy of particles from different atmospheric aerosol types. *Analytical and Bioanalytical Chemistry*, *411*(8), 1633–1645. https://doi.org/10.1007/s00216-019-01614-7

Esdaile, L. J., & Chalker, J. M. (2018). The Mercury Problem in Artisanal and Small-Scale Gold Mining. *Chemistry – A European Journal*, *24*(27), 6905–6916. https://doi.org/10.1002/chem.201704840

Gabrieli, J., Carturan, L., Gabrielli, P., Kehrwald, N., Turetta, C., Cozzi, G., Spolaor, A., Dinale, R., Staffler, H., Seppi, R., dalla Fontana, G., Thompson, L., & Barbante, C. (2011). Impact of Po Valley emissions on the highest glacier of the Eastern European Alps. *Atmospheric Chemistry and Physics*, *11*(15), 8087–8102. https://doi.org/10.5194/acp-11-8087-2011

Gabrielli, P., Cozzi, G., Torcini, S., Cescon, P., & Barbante, C. (2008). Trace elements in winter snow of the Dolomites (Italy): A statistical study of natural and anthropogenic contributions. *Chemosphere, 72*(10), 1504–1509. https://doi.org/10.1016/j.chemosphere.2008.04.076

Gaines, P. (2019). *ICP Operations Guide, A Guide for Using ICP-OES and ICP-MS*. Inorganic Ventures. https://www.inorganicventures.com/icp-guide

Goldstein, J. I., Newbury, D. E., Echlin, P., Joy, D. C., Romig, A. D., Lyman, C. E., Fiori, C., & Lifshin, E. (1992). Electron-Specimen Interactions. In *Scanning Electron Microscopy and X-Ray Microanalysis: A Text for Biologists, Materials Scientists, and Geologists* (pp. 69–147). Springer US. https://doi.org/10.1007/978-1-4613-0491-3_3

Hadley Wickham. (2016). *ggplot2: Elegant Graphics for Data Analysis*. Springer-Verlag New York. https://ggplot2.tidyverse.org

Helsel, D. (2012). *Statistics for Censored Environmental Data Using Minitab and R*. https://doi.org/10.1002/9781118162729

HiLDA. (n.d.). *About HiLDA – HiLDA*. Retrieved 7 February 2022, from https://gomera.geo.tu-darmstadt.de/wordpress/?page_id=24

Hulth, J., Rolstad, C., Trondsen, K., & Rødby, R. W. (2010). Surface mass and energy balance of Sørbreen, Jan Mayen, 2008. *Annals of Glaciology*, *51*(55), 110–119. https://doi.org/10.3189/172756410791392754

Joubert, L.-M. (2017). *Variable Pressure-SEM: a versatile tool for visualization of hydrated and non-conductive specimens.*

NIST. (2004). *1643e Standard Reference Material, Trace Elements in Water*. National Institute of Standards & Technology, Maryland, USA.

NIST. (2010). *1640a Standard Reference Material, Trace Elements in Natural Water*. National Institute of Standards & Technology, Maryland, USA.

NIST. (2015). *1643f Standard Reference Material, Trace Elements in Water*. National Institute of Standards & Technology, Maryland, USA.

NIST. (2016). *1577c Bovine Liver Certificate of Analysis Standard Reference Material*. National Institute of Standards & Technology, Maryland, USA.

Norwegian Centre for Climate Services. (2022a). *Observations and weather statistics, Jan Mayen*. https://seklima.met.no/months/max(air_temperature P1M),min(air_temperature P1M),sum(precipitation_amount P1M),max(max(wind_speed P1D) P1M),mean(air_temperature P1M)/custom_period/SN99950/en/2021-01-01T00:00:00+01:00;2021-12-31T23:59:59+01:00

Norwegian Centre for Climate Services. (2022b). *Wind rose with frequency distribution, Jan Mayen*. https://seklima.met.no/windrose/?timeresolution=custom_period&from=2021-01&to=2021-12&locationid=SN99950

Norwegian Polar Institute. (2018). *Brief Report 046—Protocols and recommendations for the measurement of snow physical properties, and sampling of snow for black carbon, water isotopes, major ions and microorganisms*. Norwegian Polar Institute, Fram Centre, NO-9296 Tromsø.

NRCC. (2008). *DORM-3. Fish Protein Certified Reference Material for Trace Metals.* National Research Council Canada, Ottawa, Canada.

NRCC. (2014). *DOLT-5 Dogfish Liver Certified Reference Material for Trace Metals and other Constituents*. National Research Council Canada, Ottawa, Canada.

OpenStreetMap contributors. (2017). *Planet dump retrieved from https://planet.osm.org*.

Pey, J., Revuelto, J., Moreno, N., Alonso-González, E., Bartolomé, M., Reyes, J., Gascoin, S., & López-Moreno, J. I. (2020). Snow Impurities in the Central Pyrenees: From

Their Geochemical and Mineralogical Composition towards Their Impacts on Snow Albedo. *Atmosphere*, *11*(9). https://doi.org/10.3390/atmos11090937

Qi, M., Jiang, L., Liu, Y., Xiong, Q., Sun, C., Li, X., Zhao, W., & Yang, X. (2018). Analysis of the Characteristics and Sources of Carbonaceous Aerosols in PM2.5 in the Beijing, Tianjin, and Langfang Region, China. *International Journal of Environmental Research and Public Health*, *15*. https://doi.org/10.3390/ijerph15071483

RStudio Team. (2020). *RStudio: Integrated Development for R*. RStudio, PBC, Boston, MA. http://www.rstudio.com/

Rury, M. (2016). *The importance of method development for trace-element analysis by inductively coupled plasma—Optical emission spectroscopy*. *31*, 16–32.

Shi, T., Cui, J., Chen, Y., Zhou, Y., Pu, W., Xu, X., Chen, Q., Zhang, X., & Wang, X. (2021). Enhanced light absorption and reduced snow albedo due to internally mixed mineral dust in grains of snow. *Atmospheric Chemistry and Physics*, *21*(8), 6035–6051. https://doi.org/10.5194/acp-21-6035-2021

Siudek, P., Frankowski, M., & Siepak, J. (2015). Trace element distribution in the snow cover from an urban area in central Poland. *Environmental Monitoring and Assessment*, *187*, 4446. https://doi.org/10.1007/s10661-015-4446-1

Skoog, D. A., Holler, F. J., & Crouch, S. R. (2017). *Principles of Instrumental Analysis* (7th ed.). Cengage Learning.

Snyder-Conn, E., Garbarino, J., Hoffman, G., & Oelkers, A. (1997). Soluble Trace Elements and Total Mercury in Arctic Alaskan Snow. *ARCTIC*, *50*. https://doi.org/10.14430/arctic1102

Soni, R., Bhardwaj, S., & Shukla, D. P. (2020). Chapter 14—Various water-treatment technologies for inorganic contaminants: Current status and future aspects. In P. Devi,

P. Singh, & S. K. Kansal (Eds.), *Inorganic Pollutants in Water* (pp. 273–295). Elsevier. https://doi.org/10.1016/B978-0-12-818965-8.00014-7

Spolaor, A., Moroni, B., Luks, B., Nawrot, A., Roman, M., Larose, C., Stachnik, Ł., Bruschi, F., Kozioł, K., Pawlak, F., Turetta, C., Barbaro, E., Gallet, J.-C., & Cappelletti, D. (2021). Investigation on the Sources and Impact of Trace Elements in the Annual Snowpack and the Firn in the Hansbreen (Southwest Spitsbergen). *Frontiers in Earth Science*, *8*. https://doi.org/10.3389/feart.2020.536036

Steffen, A., Douglas, T., Amyot, M., Ariya, P., Pfaffhuber, K. A., Berg, T., Bottenheim, J., Brooks, S., Cobbett, F., Dastoor, A., Dommergue, A., Ebinghaus, R., Ferrari, C., Gårdfeldt, K., Goodsite Ph.D., M., Lean, D., Poulain, A., Scherz, C., Skov, H., & Temme, C. (2007). A synthesis of atmospheric mercury depletion event chemistry linking atmosphere, snow and water. *Atmospheric Chemistry and Physics Discussions*, *71*. https://doi.org/10.5194/acpd-7-10837-2007

Thomas, M. A., Devasthale, A., Tjernström, M., & Ekman, A. M. L. (2019). The Relation Between Aerosol Vertical Distribution and Temperature Inversions in the Arctic in Winter and Spring. *Geophysical Research Letters*, *46*(5), 2836–2845. https://doi.org/10.1029/2018GL081624

Timmermans, R. (2022). *Studies of atmospheric dynamics from space*.

UN-Environment. (2019). *Global Mercury Assessment 2018*. UN-Environment Programme, Chemicals and Health Branch, Geneva, Switzerland. ISBN: 978-92-807-3744-8

Appendix

Appendix A

Table A1: *Overview of equipment used during sampling on Jan Mayen.*

Tools and equipment	Additional info
5 mL tubes	Sarstedt, for mercury samples
50 mL tubes	Labcon metal free tubes, for multielement samples
Blue nitril gloves	VWR, part of Avantor
Crystal card	Bought from Snowmetrics.com
Compact scale	A&D Weighing HT-3000
Cooper-Atkins Snow thermometer	Model DFP450W
Magnifying loupe	BCA, 10x magnification
Particulate free suit	VWR, part of Avantor
Respiratory mask	Medisana ®, RM 100
Snow cutters	RIP 1 Cutter (1000 cc)
Snow saw	MSR Beta™, Snow Science Saw
Snow shovel	McKinley, ref. number MK 103
Two-meter metric	Fiberglass

Table A2: *Overview of all samples collected on Jan Mayen. The asterisk indicates samples analyzed using both an inductively coupled plasma – mass spectrometer (ICP-MS) and an inductively coupled plasma – optic emission spectrometer (ICP-OES) during multielement determination. Samples marked with a number sign were analyzed both undiluted and diluted during multielement determination.*

SAMPLE NUMBER	ELEMENT DETERMINATION	CONTENT	SAMPLE TYPE	ELEVATION (M)	DATE	SNOW PIT SAMPLE DEPTH (CM)
JM-001	Hg & Multielement	Snow	Transect	2230	07.20.2021	
JM-002	Hg & Multielement	Snow	Transect	1955	07.20.2021	
JM-003	Hg & Multielement	Snow	Transect	1568	07.20.2021	
JM-004	Hg & Multielement*	Water	Around the island	4	07.25.2021	
JM-005	Hg & Multielement	Water	Around the island	14	07.25.2021	
JM-006	Hg & Multielement*	Water	Around the island	21	07.25.2021	
JM-007	Hg & Multielement*	Snow	Around the island	37	07.27.2021	
JM-008	Hg & Multielement	Water	Around the island	10	07.27.2021	
JM-009	Hg & Multielement	Snow	Transect	1302	07.28.2021	
JM-010	Hg & Multielement	Snow	Snow pit	1302	07.28.2021	0 - 5
JM-011	Hg & Multielement	Snow	Snow pit	1302	07.28.2021	5 - 10

Table A2 *continuation.*

SAMPLE NUMBER	ELEMENT DETERMINATION	CONTENT	SAMPLE TYPE	ELEVATION (M)	DATE	SNOW PIT SAMPLE DEPTH (CM)
JM-012	Hg & Multielement	Snow	Snow pit	1302	07.28.2021	10 - 15
JM-013	Hg & Multielement	Snow	Snow pit	1302	07.28.2021	15 - 20
JM-014	Hg & Multielement	Snow	Snow pit	1302	07.28.2021	20 - 25
JM-015	Hg & Multielement	Snow	Snow pit	1302	07.28.2021	25 - 30
JM-016	Hg & Multielement	Snow	Snow pit	1302	07.28.2021	30 - 35
JM-017	Hg & Multielement	Snow	Snow pit	1302	07.28.2021	35 - 40
JM-018	Multielement	Snow	Snow pit	1302	07.28.2021	40 - 45
JM-019	Hg & Multielement	Snow	Snow pit	1302	07.28.2021	45 - 50
JM-020	Hg & Multielement	Snow	Snow pit	1302	07.28.2021	50 - 55
JM-021	Hg & Multielement	Snow	Snow pit	1302	07.28.2021	55 - 60
JM-022	Hg & Multielement	Snow	Snow pit	1302	07.28.2021	60 - 65
JM-023	Hg & Multielement	Snow	Snow pit	1302	07.28.2021	65 - 70
JM-024	Hg & Multielement	Snow	Snow pit	1302	07.28.2021	70-75
JM-025	Hg & Multielement	Snow	Snow pit	1302	07.28.2021	75 - 80
JM-026	Hg & Multielement	Snow	Snow pit	1302	07.28.2021	80 - 85
JM-027	Hg & Multielement	Snow	Snow pit	1302	07.28.2021	85 - 90
JM-028	Hg & Multielement	Snow	Snow pit	1302	07.28.2021	90 - 95
JM-029	Hg & Multielement	Snow	Field blank	1302	07.28.2021	
JM-030	Hg & Multielement	Snow	Field blank	1302	07.28.2021	
JM-031	Hg & Multielement	Snow	Field blank	1302	07.28.2021	
JM-032	Hg & Multielement	Snow	Field blank	1302	07.28.2021	
JM-033	Hg & Multielement	Snow	Field blank	1302	07.28.2021	
JM-034	Hg & Multielement	Snow	Field blank	1302	07.28.2021	
JM-035	Hg & Multielement	Snow	Field blank	1302	07.28.2021	
JM-036	Hg & Multielement	Snow	Transect	1114	07.28.2021	
JM-037	Hg & Multielement	Snow	Transect	1101	07.28.2021	
JM-038	Hg & Multielement	Snow	Transect	999	07.28.2021	
JM-039	Hg & Multielement	Snow	Transect	907	07.28.2021	
JM-040	Hg & Multielement*	Snow	Transect	800	07.28.2021	
JM-041	Hg & Multielement	Snow	Transect	701	07.28.2021	
JM-042	Hg & Multielement*	Snow	Transect	512	07.29.2021	
JM-043	Multielement	Snow	Transect	512	07.29.2021	
JM-044	Hg & Multielement*	Snow	Transect	512	07.29.2021	
JM-046	Hg & Multielement*	Snow	Transect	0	07.29.2021	
JM-047	Hg & Multielement	Snow	Transect	587	07.28.2021	
JM-048	Hg & Multielement	Snow	Transect	512	07.28.2021	
JM-049	Hg & Multielement	Snow	Transect	512	07.29.2021	
JM-050	Hg & Multielement	Snow	Transect	512	07.29.2021	
JM-051	Multielement	Snow	Around the island	505	07.31.2021	
JM-052	Hg & Multielement	Snow	Around the island	545	07.31.2021	

Table A2 *continuation.*

SAMPLE NUMBER	ELEMENT DETERMINATION	CONTENT	SAMPLE TYPE	ELEVATION (M)	DATE	SNOW PIT SAMPLE DEPTH (CM)
JM-053	Hg & Multielement*	Snow	Around the island	388	07.31.2021	
JM-054	Hg & Multielement*	Snow	Around the island	79	08.01.2021	
JM-055	Hg & Multielement	Snow	Around the island	253	08.02.2021	
JM-056	Hg & Multielement	Water	Around the island	490	08.02.2021	
JM-057	Hg & Multielement*	Snow	Around the island	394	08.02.2021	
JM-058	Hg & Multielement*#	Water	Around the island	0	08.03.2021	
JM-059	Hg & Multielement*#	Water	Around the island	1	08.03.2021	
JM-060	Hg & Multielement*#	Water	Around the island	0	08.03.2021	
JM-061	Multielement	Water	Around the island	411	08.04.2021	
JM-062	Hg & Multielement*	Snow	Transect	412	08.04.2021	
JM-063	Hg & Multielement*	Snow	Transect	306	08.04.2021	
JM-064	Hg & Multielement*	Snow	Transect	222	08.04.2021	
JM-065	Hg & Multielement*	Snow	Transect	139	08.04.2021	
JM-066	Hg & Multielement*	Water	Around the island	2	08.05.2021	
JM-067	Hg & Multielement*	Water	Around the island	9	08.05.2021	
JM-068	Hg & Multielement*#	Water	Around the island	170	08.05.2021	
JM-069	Hg & Multielement*#	Water	Around the island	10	08.05.2021	
JM-070	Hg & Multielement*	Water	Around the island	319	08.06.2021	
JM-071	Hg & Multielement*	Snow	Around the island	322	08.06.2021	
JM-072	Hg & Multielement*	Water	Around the island	319	08.06.2021	
JM-073	Multielement*	Snow	Around the island	198	08.10.2021	

Table A3: *Overview of differences in sample tubes, volumes etc. between the mercury and multielement determinations.*

	SAMPLE TUBES	TUBE VOLUME	STOCK ACID CONCENTRATION	ACID CONCENTRATION IN SAMPLES	ICP-MS MODEL
MERCURY DETERMINATION	Sarstedt	5 mL	37% HCl (w/w), 69% HNO_3 (w/w)	2% (V/V) HCl, 5% (V/V) HNO_3	Perkin Elmer ICP-MS 8800
MULTIELEMENT DETERMINATION	Labcon®	50 mL	69% HNO_3 (w/w)	1% (V/V) HNO_3	Perkin Elmer ICP-MS 8900

Table A4: *Instrumental settings for different parameters used in mercury analyses using an Agilent 8800 ICP-MS.*

Parameter	Setting	
Scan type	MS/MS	
Monitored mass pairs (Q1 → Q2):	202 → 202	($^{202}Hg^+ \rightarrow {}^{202}Hg^+$)
Integration time [sec]	0.4500	
Replicates	10	
RF Power [W]	1600	
Sample depth plasma [mm]	8.0	
Nebulizer gas flow [L min^{-1}]	1.30	
Spray chamber temperature [°C]	17	
Collision-reaction cell:		
Octopole bias [V]	-8.0	
Axial acceleration [V]	No-gas: 0, He: 1, O_2: 1.5, NH_3: 0.5	
Energy discrimination [V]	5.0	
Deflect lens [V]	14.4	

Table A5: *Overview of all standards used. Product number, elements contained, producer and method of analysis is given.*

STANDARD (PRODUCT NUMBER)	ELEMENTS	MANUFACTURER	METHOD OF ANALYSIS
IV-ICPMS-71A	Ag, Al, As, B, Ba, Be, Ca, Cd, Ce, Co, Cr, Cs, Du, Dy, Er, Eu, Fe, Ga, Gd, Ho, K, La, Lu, Mg, Mn, Na, Nd, Ni, P, Pb, Pr, Rb, S, Se, Sm, Sr, Th, Tl, Tm, U, V, Yb, Zn	Inorganic Ventures	ICP-MS
IV-ICPMS-71B	Ge, Hf, Mo, Nb, Sb, Si, Sn, Ta, Te, Ti, W, Zr	Inorganic Ventures	ICP-MS
CGHG1-1	Hg	Inorganic Ventures	ICP-MS
SS-10212	Al	Spectrascan	ICP-MS/ICP-OES
SS-1216	Ba	Spectrascan	ICP-MS/ICP-OES
SS-10206	Ca	Spectrascan	ICP-MS/ICP-OES
SS-1501	Cu	Spectrascan	ICP-MS/ICP-OES
CGFE1-5	Fe	Inorganic Ventures	ICP-MS/ICP-OES
CGMG10	Mg	Inorganic Ventures	ICP-MS/ICP-OES
455644H	Mn (certified)	VWR Chemicals	ICP-MS/ICP-OES
CGP1	P	Inorganic Ventures	ICP-MS/ICP-OES
CGK10-5	K	Inorganic Ventures	ICP-MS/ICP-OES
8054	Se (certified)	Spectrascan	ICP-MS
CGNA10	Na	Inorganic Ventures	ICP-MS/ICP-OES
CGSR1	Sr	Inorganic Ventures	ICP-MS/ICP-OES
CGMSA10-5	S	Inorganic Ventures	ICP-MS/ICP-OES
CGZN1	Zn	Inorganic Ventures	ICP-MS/ICP-OES
SS-1215	B	Spectrascan	ICP-MS
CGSI1	Si	Inorganic Ventures	ICP-MS/ICP-OES
SS-1264	Ti	Spectrascan	ICP-MS/ICP-OES
SS-1238	Li	Spectrascan	ICP-MS
CGTB-1	Tb (certified)	Inorganic Ventures	ICP-MS
1068-5	V	Spectrascan	ICP-OES
S-CR-1.250	Cr (certified)	Spectrapure Standards	ICP-OES
SS-1208	Co	Spectrascan	ICP-OES
S-NI-1.250	Ni (certified)	Spectrapure Standards	ICP-OES
8048	Rb	Spectrascan	ICP-OES
SS-1270	Y	Spectrascan	ICP-OES
1203	$LaCl_3$	Spectrascan	ICP-OES
CGND1-1	Nd	Inorganic Ventures	ICP-OES

Table A6: *Concentrations of standards used in the multielement analysis with the ICP-MS. The concentration ratio between the two standards were 1:10.*

ELEMENT	STD 1 (µg/L)	STD 2 (µg/L)
Li	0.2	2
Be	0.2	2
B	10	100
Na	1	10
Mg	0.2	2
Al	100.2	1002
Si	200.2	2002
P	200.2	2002
S	0.5	5
K	0.2	2
Ca	1	10
Sc	0.2	2
Ti	20.2	202
V	0.2	2
Cr	0.2	2
Mn	5.2	52
Fe	100.2	1002
Co	0.2	2
Ni	0.2	2
Cu	2.2	22
Zn	2.2	22
Zn	2.2	22
Ga	0.2	2
Ge	0.2	2
As	0.2	2
Se	2.2	22
Rb	0.2	2
Sr	2.2	22
Y	0.2	2
Zr	0.2	2
Nb	0.2	2
Mo	0.2	2
Ag	0.2	2
Cd	0.2	2
Sn	0.2	2
Sb	0.2	2
Te	0.2	2
Cs	0.2	2
Ba	2.2	22
La	0.2	2

***TABLE A6** continuation.*

ELEMENT	STD 1 (µg/L)	STD 2 (µg/L)
Ce	0.2	2
Pr	0.2	2
Nd	0.2	2
Sm	0.2	2
Eu	0.2	2
Gd	0.2	2
Tb	0.2	2
Dy	0.2	2
Ho	0.2	2
Er	0.2	2
Tm	0.2	2
Yb	0.2	2
Lu	0.2	2
Hf	0.2	2
Ta	0.2	2
W	0.2	2
Tl	0.2	2
Pb	0.2	2
Th	0.2	2
U	0.2	2

***Table A7:** Elements determined during the multielement analysis using an 8900 Agilent ICP-MS. *Internal standard.*

GAS MODE	$^{MASS \rightarrow MASS}$ELEMENT
NO GAS	^{7}Li, ^{9}Be, ^{11}B, ^{103}Rh*, ^{115}In*, ^{118}Sn, ^{209}Bi*, ^{232}Th, ^{238}U
He	^{23}Na, ^{24}Mg, ^{27}Al, ^{39}K, ^{52}Cr, ^{55}Mn, ^{56}Fe, ^{58}Ni, ^{59}Co, ^{60}Ni, ^{63}Cu, ^{64}Zn, ^{65}Cu, ^{66}Zn, ^{85}Rb, ^{88}Sr, ^{89}Y, ^{103}Rh*, ^{115}In*, ^{118}Sn, ^{209}Bi*
O_2	$^{28\rightarrow44}$Si, $^{29\rightarrow45}$Si, $^{31\rightarrow47}$P, $^{32\rightarrow48}$S, $^{34\rightarrow50}$S, $^{44\rightarrow60}$Ca, $^{45\rightarrow61}$Sc, $^{47\rightarrow63}$Ti, $^{51\rightarrow67}$V, $^{72\rightarrow78}$Ge, $^{75\rightarrow91}$As, $^{78\rightarrow94}$Se, $^{89\rightarrow105}$Y, $^{90\rightarrow106}$Zr, $^{93\rightarrow125}$Nb, $^{95\rightarrow127}$Mo, $^{97\rightarrow129}$Mo, ^{103}Rh*, $^{107\rightarrow107}$Ag, $^{111\rightarrow111}$Cd, $^{114\rightarrow114}$Cd, ^{115}In*, $^{118\rightarrow118}$Sn, $^{121\rightarrow121}$Sb, $^{125\rightarrow125}$Te, $^{139\rightarrow155}$La, $^{140\rightarrow156}$Ce, $^{141\rightarrow157}$Pr, $^{146\rightarrow162}$Nd, $^{147\rightarrow163}$Sm, $^{151\rightarrow151}$Eu, $^{151\rightarrow167}$Eu, $^{157\rightarrow173}$Gd, $^{159\rightarrow175}$Tb, $^{163\rightarrow179}$Dy, $^{165\rightarrow181}$Ho, $^{166\rightarrow182}$Er, $^{169\rightarrow185}$Tm, $^{172\rightarrow172}$Yb, $^{175\rightarrow191}$Lu, $^{178\rightarrow194}$Hf, $^{181\rightarrow213}$Ta, $^{182\rightarrow214}$W, ^{209}Bi*, $^{232\rightarrow264}$Th, $^{238\rightarrow270}$U
NH_3	^{24}Mg, ^{27}Al, ^{39}K, $^{45\rightarrow130}$Sc, ^{52}Cr, ^{55}Mn, ^{56}Fe, ^{58}Ni, ^{59}Co, ^{60}Ni, ^{63}Cu, ^{64}Zn, ^{65}Cu, ^{66}Zn, ^{71}Ga, ^{85}Rb, ^{88}Sr, $^{89\rightarrow191}$Y, ^{103}Rh*, ^{115}In*, ^{118}Sn, ^{121}Sb, ^{133}Cs, ^{137}Ba, ^{205}Tl, ^{206}Pb, ^{207}Pb, ^{208}Pb, ^{209}Bi*

Table A8: *Instrumental settings for different parameters used in multielement analysis using ICP-MS.*

PARAMETER	SETTING	
SCAN TYPE	MS/MS	
MONITORED MASS PAIRS (Q1 → Q2):	11 → 11	($^{11}B^+ \rightarrow {}^{11}B$)
	103 → 103	($^{130}Rh^+ \rightarrow {}^{130}Rh^+$)
	232 → 232	($^{232}Th^+ \rightarrow {}^{232}Th^+$)
	238 → 238	($^{238}U^+ \rightarrow {}^{238}U^+$)
INTEGRATION TIME	0.1500 sec for No gas-mode and He-mode; 0.2000 sec O_2-mode and NH_3-mode.	
REPLICATES	6	
RF POWER [W]	1600	
SAMPLE DEPTH PLASMA [mm]	7.5	
NEBULIZER GAS FLOW [L min^{-1}]	1.05	
SPRAY CHAMBER TEMPERATURE [°C]	2	
COLLISION-REACTION CELL:		
O_2 FLOW RATE [mL min^{-1}]	0.525	
HE FLOW RATE [mL min^{-1}]	5	
NH_3 FLOW RATE [mL min^{-1}]	3.5	
OCTOPOLE BIAS [V]	No-gas: -8.0, He: -18.0, O_2: -3.0, NH_3: -5.0	
AXIAL ACCELERATION [V]	No-gas: 0, He: 1, O_2: 1.5, NH_3: 0.5	
ENERGY DISCRIMINATION [V]	No-gas: 5.0, He: 5.0, O_2: -7.0, NH_3: -7.0	
DEFLECT LENS [V]	No-gas: 12.2, He: -2.4, O_2: 6.6, NH_3: 3.0	

Table A9: *Instrumental settings for different parameters used in for multielement analysis using ICP-OES.*

PARAMETER	SETTING
Read Time [sec]	5
Rf Power [kW]	1.50
Viewing Mode	Radial
Viewing Height [mm]	3
Replicates	3
Pump Speed [rpm]	10
Rinse Time [sec]	7

Table A10: *Overview of elements with corresponding wavelengths used in the ICP-OES-analysis, as well as standard concentrations.*

Element	Wavelength (nm)	Std 1 (mg/L)	Std 2 (mg/L)	Std 3 (mg/L)
Al	167.019	2.0	10	20
Al	396.152	2.0	10	20
Ba	455.403	0.02	0.10	0.20
Ba	493.408	0.020	0.10	0.20
Ca	393.366	2.0	10	20
Ca	422.673	2.0	10	20
Ce	418.659	-	0.10	0.20
Co	228.615	-	0.10	0.20
Cr	267.716	0.020	0.10	0.20
Fe	238.204	2.0	10	20
K	766.491	5.0	25	50
La	333.749	0.020	0.10	0.20
Mg	280.270	5.0	25	50
Mn	259.372	0.20	1.0	2.00
Na	589.592	10	50	100
Nd	401.224	-	0.10	0.20
Ni	216.555	-	0.10	0.20
P	178.222	1.0	5.000	10
P	213.618	1.0	5.000	10
S	181.972	1.0	5.000	10
Si	251.611	2.0	10	20
Sr	407.771	0.020	0.10	0.20
Ti	334.941	0.20	1.0	2.0
V	292.401	0.050	0.25	0.50
Y	360.074	0.020	0.10	0.20
Zn	206.200	0.020	0.10	0.20

Appendix B

Table B1: *The table presents detection limits (LOD) and quantification limits (LOQ) for every element determined in this thesis. The limits are calculated from the standard deviation of the seven field blanks.*

Element	LOD (µg/L)	LOQ (µg/L)	Element	LOD (µg/L)	LOQ (µg/L)
Li	0.005	0.016	Mo	0.0008	0.0026
Be	0.0002	0.00063	Ag	0.0007	0.0022
B	2	6.4	Cd	0.0002	0.00074
Na*	3	10	Sn	0.002	0.0057
Mg*	0.09	0.29	Sb	0.0002	0.0008
Al	0.4	1.2	Te	0.0001	0.00049
Si	9	31	Cs	0.0003	0.00095
P	0.2	0.64	Ba	0.03	0.095
S*	0. 3	1.1	La	0.00007	0.00025
K*	3	9.9	Ce	0.0001	0.00048
Ca*	1	4.4	Pr	0.00005	0.00017
Sc	0.0003	0.00088	Nd	0.0001	0.00036
Ti	0.02	0.05	Sm	0.0002	0.00061
V	0.0004	0.0014	Eu	0.00003	0.000087
Cr	0.02	0.062	Gd	0.00006	0.00019
Mn	0.008	0.025	Tb	0.00003	0.000093
Fe	0.3	1	Dy	0.00006	0.0002
Co	0.0005	0.0017	Ho	0.00003	0.00011
Ni	0.02	0.056	Er	0.00007	0.00024
Cu	0.05	0.18	Tm	0.00004	0.00015
Zn	0.05	0.17	Yb	0.00007	0.00024
Ga	0.0004	0.0013	Lu	0.00007	0.00022
Ge	0.001	0.0043	Hf	0.0001	0.00039
As	0.0002	0.00065	Ta	0.00006	0.0002
Se	0.007	0.022	W	0.0001	0.00035
Rb	0.002	0.0061	Hg	0.00027	0.00090
Sr	0.001	0.0046	Tl	0.0002	0.00072
Y	0.00006	0.0002	Pb	0.02	0.066
Zr	0.0001	0.0005	Th	0.00008	0.00027
Nb	0.0003	0.00091	U	0.00009	0.00029

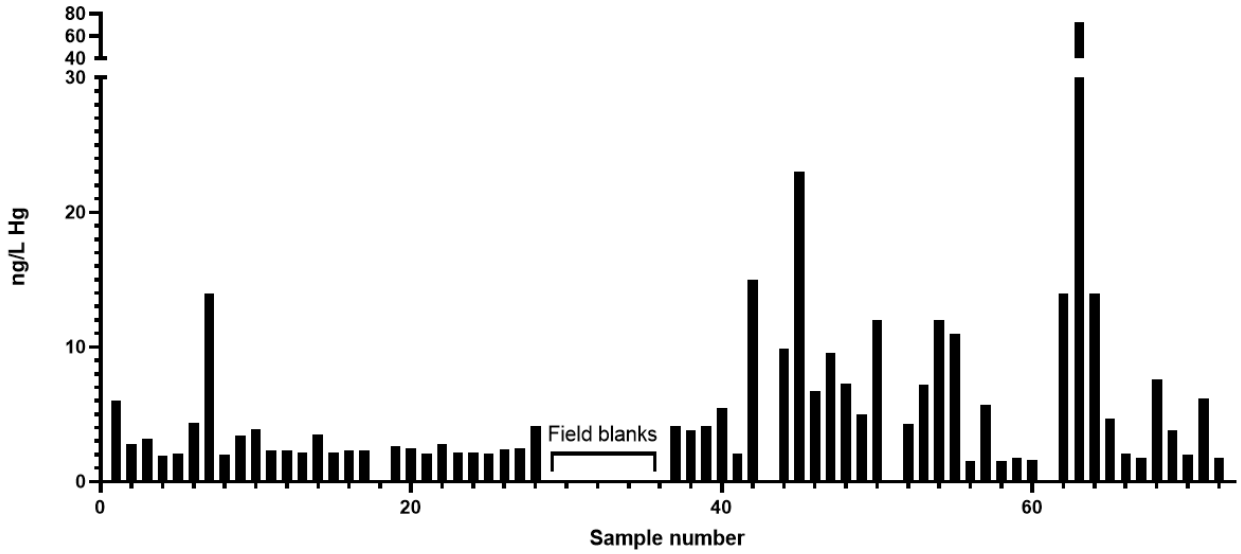

Figure B1*: The figure presents the mercury concentrations determined for each sample using an ICP-MS. Sample 29 to 35 are field blanks.*

Appendix C

Figure C1: *Photo of Jan Mayen depicting the snow-covered volcano and barren landscape at lower altitudes. Photography taken by Stine Eriksen Hammer (2021).*

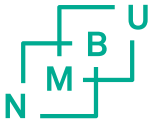

Norges miljø- og biovitenskapelige universitet
Noregs miljø- og biovitskapelege universitet
Norwegian University of Life Sciences

Postboks 5003
NO-1432 Ås
Norway